Department of Physics and Astronomy
University of Heidelberg

Bachelor's Thesis in Physics
submitted by

Henning Mescher

born in Weilburg an der Lahn (Germany)

July 2014

Evaluation of uncertainty in linear energy transfer calibration of Al_2O_3:C,Mg-based fluorescent nuclear track detectors

This Bachelor's Thesis has been carried out by Henning Mescher at the
DKFZ Heidelberg
under the supervision of
Prof. Dr. rer. nat. Peter Bachert
and
Prof. Dr. rer. nat. Oliver Jäkel

Fluorescent nuclear track detectors (FNTDs), a novel biocompatible detector type, represent possible candidates for the application in medical physics research. Besides recording the particle fluence, they allow for energy deposition quantification, i.e. linear energy transfer (LET) determination by measuring the fluorescence signal. A correlation between LET and measured fluorescence intensity was already observed but suffers, especially concerning the clinical LET range, from large variabilities. Since a precise relation between those two quantities is still desirable, the aim of this Bachelor's thesis was to evaluate different sources of uncertainty regarding the measured fluorescence intensity. Therefore, a set of 66 detectors was irradiated with mono-energetic particle beams covering a LET range of $1 - 150\,\frac{\mathrm{keV}}{\mu\mathrm{m}}$. This results in 22 data points with different LET values consisting of each three irradiated detectors. Intensity measurements were performed using a commercial confocal laser-scanning microscope. The read out of this set of detectors enables to investigate microscope and detector related fluctuations. Different read out days and the read out with different laser powers influence the resulting fluorescence signals only slightly. Regarding detector related fluctuations, the evaluation shows decreasing relative intra-image fluctuations related to the stochastic nature of energy deposition with rising LET. Investigations concerning different read out positions within the detectors result in relative fluctuations of approximately 4%, whereas relative inter-detector variabilities are much larger and lie in the magnitude of 16%. Finally, the measured intensities and the evaluation of the different sources of uncertainty were used to establish a LET-fluorescence relation.

Biokompatible, fluoreszierende Kernspurdetektoren (FNTDs) könnten aufgrund ihrer Eigenschaften in der medizinphysikalischen Forschung eingesetzt werden. Mithilfe von Fluoreszenzmessungen erlauben diese Detektoren neben einer präzisen Bestimmung der Teilchenfluenz außerdem eine Quantifizierung des Energieverlustes, d.h. des linearen Energietransfers (LET). Eine Korrelation zwischen der gemessenen Fluoreszenz und dem Energieverlust der Teilchen wurde bereits beobachtet. Die Resultate sind allerdings, vor allem im klinischen LET-Bereich, starken Schwankungen hinsichtlich der gemessenen Intensität unterworfen und eine Kalibrierung mit verbesserter Präzision ist wünschenswert. Ziel dieser Bachelorarbeit war es deshalb, die verschiedenen Fehlerquellen hinsichtlich der gemessen Intensität zu bestimmen und zu quantifizieren. Zu diesem Zweck wurde ein Satz von 66 Detektoren mit verschiedenen LETs im Bereich von $1 - 150\,\frac{\mathrm{keV}}{\mu\mathrm{m}}$ bestrahlt. Daraus ergaben sich 22 LET-Datenpunkte, die aus jeweils drei bestrahlten Detektoren bestehen. Fluoreszenzmessungen an diesem Detektorsatz wurden mithilfe eines kommerziell erhältlichen konfokalen Mikroskops durchgeführt und ermöglichten eine Analyse der verschiedenen Einflussfaktoren. Untersuchungen bezüglich des Ausleseprozesses, d.h. Messungen an verschiedenen Tagen und Fluoreszenzbestimmungen unter der Verwendung verschiedener Laserstärken, zeigten lediglich einen geringen Einfluss. Anders verhielt es sich mit detektor-bedingten Intensitätschwankungen. Relative Schwankungen im Fluoreszensignal innerhalb eines Mirkoskopbildes werden durch die stochastische Energieabgabe der geladenen Teilchen hervorgerufen und fielen mit steigendem LET der Teilchen stark ab. Relative Schwankungen im Fluoreszenzsignal innerhalb eines Detektors lagen im Bereich von 4%, wohingegen Intensitätschwankungen zwischen verschiedenen Detektoren in der Größenordnung von 16% gemessen wurden. Die gemessenen Intensitäten und die Untersuchung der einzelnen Einflussfaktoren wurden abschließend verwendet, um einen funktionalen Zusammenhang zwischen LET und der gemessenen Fluoreszenzintensität zu bestimmen.

Contents

1 Introduction

Radiation therapy commonly uses ionizing radiation, such as photons or electrons, for the treatment of malignant tumors. However, the use of charged particles such as protons and heavier ions has gained increasing importance over the last few years [1].

Besides the improved dose delivery due to their inverse depth-dose profile, such beams have the potential advantage of an increased biological effectiveness compared to conventionally applied therapies at the same dose [2]. This effect depends on the charge and the energy of the ions present in the beam. Thus, one must be able to determine the particle and the energy spectrum of such ion beams to predict its biological effect. Hence, novel detectors are required for the application in medical physics research. Fluorescent nuclear track detectors (FNTDs) represent possible candidates, as they allow for quantification of the particle fluence [3] as well as of the energy deposition, i.e. linear energy transfer (LET) [4,5]. The measured fluorescence signal of FNTDs is proportional to the energy loss of a traversing ion. A correlation between those quantities had been established but mainly for higher LETs [4] or suffering - for the clinically relevant LETs - from large variabilities [5]. However, a reliable, more accurate LET-fluorescence relation of clinical energies is still desirable. Therefore, the aim of this Bachelor's thesis was to identify and potentially quantify the major sources of uncertainty concerning the measured fluorescence signal.

In order to achieve this aim, a set of 66 detectors was irradiated with mono-energetic beams of protons, helium, carbon and oxygen ions ranging from $1 - 150\,\frac{\mathrm{keV}}{\mu\mathrm{m}}$. Analysis of the magnitude and influence of microscope and detector related variability yielded an improved LET-fluorescence correlation.

Physical background knowledge and the relevant quantities are introduced in chapter 2. The following chapter 3 contains a detailed depiction of the utilized detectors. Furthermore, the irradiation and read out facility, the software for the data evaluation as well as the required data generation is presented. In chapter 4 the different performed investigations concerning different sources of variabilities are documented. Chapter 5 and chapter 6 finally discuss the obtained results and give an conclusion with an outlook regarding further experiments.

2 Physical Background

2.1 Particle fluence

Fluorescent nuclear track detectors (FNTDs) primarily record the particle fluence Φ. Generally, the particle fluence $\Phi(\mathbf{r})$ at the position $\mathbf{r}$ is defined as the quotient of the number of particles $\mathrm{d}N$ passing through an infinitesimal area $\mathrm{d}A_\perp$:

$$\Phi(\mathbf{r}) = \frac{\mathrm{d}N}{\mathrm{d}A_\perp} \tag{2.1}$$

The reference plane $\mathrm{d}A_\perp$ describes the cross sectional area of an infinitesimal sphere surrounding $\mathbf{r}$, that is respectively orientated perpendicular to the propagation of the particles [6]:

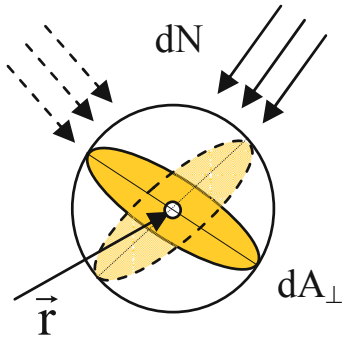

Figure 2.1 – Schematic illustration of the particle fluence definition. The infinitesimal sphere surrounding $\mathbf{r}$ and the respective to the propagation of the particles orientated reference plane $\mathrm{d}A_\perp$ are illustrated. The quotient of the number of particles $\mathrm{d}N$ passing through $\mathrm{d}A_\perp$ defines the particle fluence at the position $\mathbf{r}$. Reprinted from [6].

In the case of unidirectional, homogeneous and orthogonally impinging particle beams, which applies for all irradiations in this thesis, the fluence Φ can be simplified to:

$$\Phi = \frac{N}{A} \tag{2.2}$$

where N represents the total number of particles passing through the finite area A.

2.2 Mass stopping power

The energy loss of charged particles to matter can be described by the mass stopping power $\frac{S}{\rho}$, defined as the mean energy $\mathrm{d}E$ lost per path length $\mathrm{d}l$ in the material of density

ρ [7]:

$$\frac{S}{\rho} = \frac{1}{\rho}\frac{\mathrm{d}E}{\mathrm{d}l} \tag{2.3}$$

The mass stopping power consists of three major independent components:

$$\frac{S}{\rho} = \frac{1}{\rho}\left(\frac{\mathrm{d}E}{\mathrm{d}l}\right)_{el} + \frac{1}{\rho}\left(\frac{\mathrm{d}E}{\mathrm{d}l}\right)_{rad} + \frac{1}{\rho}\left(\frac{\mathrm{d}E}{\mathrm{d}l}\right)_{nuc} = \frac{1}{\rho}\left(S_{el} + S_{rad} + S_{nuc}\right) \tag{2.4}$$

where S_{el} is the electronic stopping power due to interactions with atomic electrons, S_{rad} is the radiative stopping power due to emission of bremsstrahlung, and S_{nuc} is the nuclear stopping power due to elastic Coulomb interactions with the target nuclei [7].

Radiation therapy requires ion beam ranges in tissue of $2 - 30\,\mathrm{cm}$, corresponding to velocities of up to $\beta = v/c \approx 0.7$. The energy loss at these velocities is dominated by interactions with target electrons, thus by S_{el} [8]. The slow down of particles in matter caused by their loss of energy lead to a broadened velocity distribution within clinical ion beams.

2.3 Nuclear interaction

While the stopping process of ion beams in the case of clinical energies is governed by electronic interactions, the probability of nuclear interactions is much smaller. Nonetheless, this interaction leads partly to fragmentation resulting in a loss of primary beam particles and a build-up of lower-Z fragments [8]. As a result, the beam consists of a particle spectrum with different energies and different Z.

2.4 Electronic stopping power

The electronic stopping power S_{el} can be described by the Bethe formula [8]:

$$S_{el} = \left(\frac{\mathrm{d}E}{\mathrm{d}l}\right)_{el} \propto \frac{Z_t}{A_t}\frac{Z_p^2}{\beta^2}L(\beta) \tag{2.5}$$

where Z_t and A_t are the atomic number and relative atomic mass of the target material, L is the stopping number, β is the particle velocity in units of the velocity of light and Z_p is the charge of the particle [9]. Since the energy loss of charged particles traversing through matter is of stochastic nature, the Bethe equation describes the mean energy loss by interactions with target electrons [10]. The stochastic nature regarding the energy deposition is sometimes referred to as the energy loss straggling of a particle.
In this thesis always the same detector material (Al_2O_3) was irradiated. Hence, target specific quantities such as Z_t and A_t are only important when stopping powers were converted to the corresponding quantity in water. Thus, S_{el} mainly depends on the particle type Z_p and its velocity β. The spread in the particle and energy spectrum lead

to a broad spectrum of different stopping powers S_{el} in clinical ion beams. Since the relative biological effectiveness (RBE) of such beams depends on S_{el}, it is inevitable to measure the entire stopping power spectrum for beam characterization. FNTDs represent possible candidates for such measurements since their detection principle is based on trapping electrons [11] liberated in the electronic stopping processes. Furthermore, they have a wide range of sensitivity [12].

2.5 Linear energy transfer

The linear energy transfer (LET), also known as restricted electronic stopping power L_Δ, refers to the mean energy loss $\mathrm{d}E_\Delta$ due to electronic interactions in traversing a distance $\mathrm{d}l$ excluding all kinetic energies of released electrons greater than Δ [7]:

$$L_\Delta = \frac{\mathrm{d}E_\Delta}{\mathrm{d}l} \quad \text{with} \quad \lim_{\Delta\to\infty} L_\Delta = S_{el} \tag{2.6}$$

Thus, the LET describes the local energy deposition of particles interacting with target electrons as electrons with kinetic energies greater than Δ deposit their energy far from the particle's track. In this thesis the intensity of single particle tracks, detected with FNTDs, represent the basis of all investigations. The detected signal rather refers to the restricted LET than to S_{el} of the charged particle. Since the restricted and the unrestricted LET differ only slightly for the performed irradiations in this thesis, and in addition, for clinical ion beams, the energy loss of charged particles is dominated by the electronic stopping process, we assume:

$$L_\Delta \approx L_\infty \quad , \quad S_{el} \approx \left(\frac{\mathrm{d}E}{\mathrm{d}l}\right)_{\text{clinical}} \tag{2.7}$$

The terms linear energy transfer, electronic stopping power and energy loss are used synonymously.

3 Material and Methods

3.1 Fluorescent nuclear track detectors

Fluorescent nuclear track detectors (FNTDs) developed by Landauer Inc. (Stillwater, USA) are a biocompatible detector type [13] consisting of aluminum oxide crystals doped with carbon and magnesium [14]. The detector material was originally developed for volumetric optical data storage [15]. However, further research showed that oxygen vacancies inside the crystals enable also storage of dose information of traversing particles by capturing excited electrons [11]. Due to their superior spatial imaging resolution and wide range of LET sensitivity, FNTDs have advantages over conventionally used plastic nuclear track detectors (PNTDs) [12]. For this study 66 detectors with dimensions of $4 \times 8\,\mathrm{mm}^2$ and 0.5 mm thickness with the long side aligned to the optical c-axis were utilized. Fig. 3.1 illustrates the size of the used FNTDs compared to an Euro Cent. To enable the optical read out with a confocal microscope, one of the large areas is polished to high optical quality.

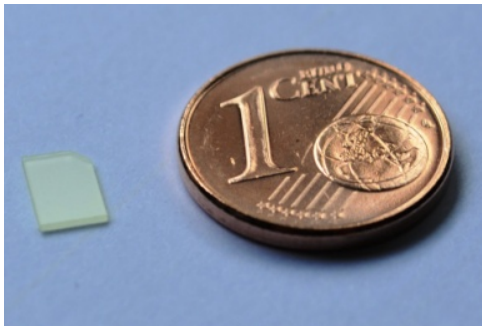

Figure 3.1 – Green colored FNTDs with dimensions ($4 \times 8 \times 0.5\,\mathrm{mm}^3$) compared to the size of an Euro Cent. One large surface is polished to obtain an optically transparent surface. Reprinted from [16].

3.1.1 Crystal structure of Al_2O_3:C,Mg

Aluminum oxide forms the basis of FNTDs, commonly occurs as α-Al_2O_3, and consists of a hexagonal-closed-packed O^{2-} sub-lattice. Two-thirds of the octahedral interstices are occupied by a Al^{3+} ion. This results in six O^{2-} surrounding one Al^{3+} ion. Fig. 3.2a shows the basic structure of this rigid and slightly distorted lattice [17].

To enable the storage of dose information, color centers (F centers) consisting of oxygen vacancies are created during crystal growth in a highly reducing atmosphere [15]. Those oxygen vacancies result in a strong local charge imbalance and function, therefore, as trap for electrons. F^{2+} indicates a vacancy without an electron, whereas F^{+} and F stand for one and two-electron states. Depending on the number of trapped electrons in one vacancy, the resulting F center have different fluorescence properties [18]. This enables to quantify the production of secondary electrons by ionizing particles.

Doping aluminum oxide with carbon and magnesium leads to a preferred production of complex F^{+} centers since they are required for the charge compensation of Mg^{2+} ions. Fig. 3.2b illustrate the structure of Al_2O_3:C,Mg. Two F^{+} centers form in combination with two Mg^{2+} ions a two electron F_2^{2+}(2Mg) state [17]. The concentration of those F_2^{2+}(2Mg) centers is also referred to as the colorization of the detector and quantify its sensitivity. Caused by inevitable processes during the crystal growth, the colorization as well as the sensitivity may vary within the same detectors and between different detectors.

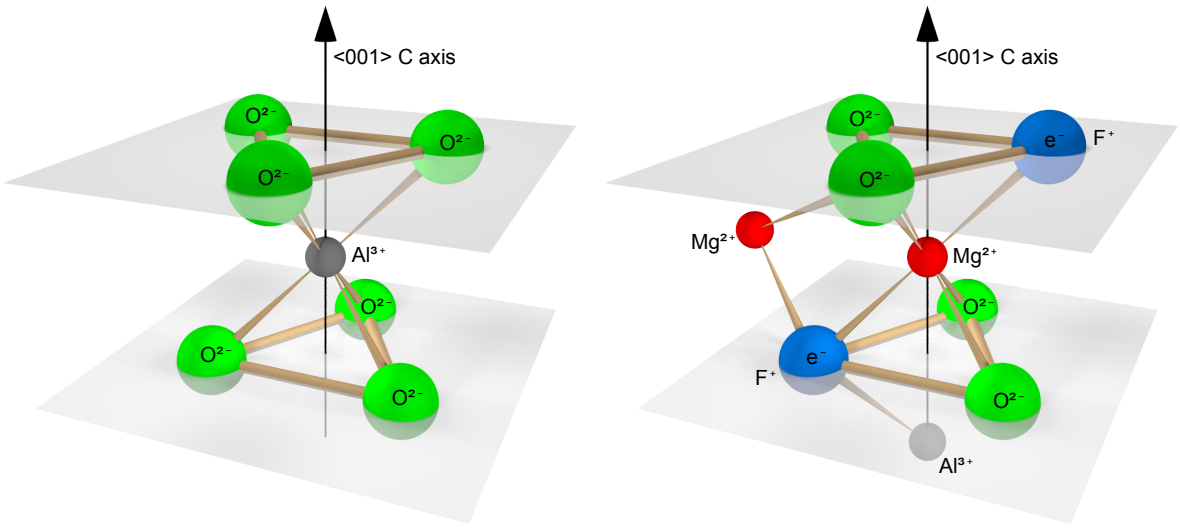

(a) Crystal structure of α-Al_2O_3 **(b)** Crystal structure of Al_2O_3:C,Mg

Figure 3.2 – Illustration of the crystal structure of aluminum oxide with orientation of the optical c-axis before (a) and after doping (b) with magnesium and carbon. Two F^{+} centers form in combination with two Mg^{2+} ions a F_2^{2+}(2Mg) color center. Reproduced according to [17].

3.1.2 Radiochromic transformation and fluorescence

The different F centers inside the crystal are characterized by different absorption bands [18]. For the usage as particle detector, mainly created F_2^{2+}(2Mg) centers and their transformations are of particular interest. Ionizing radiation produces free electrons in

the conduction band of the crystal. $F_2^{2+}(2Mg)$ centers are able to capture those electrons due to local charge imbalances. This leads to a radiochromic transformation and forms a three electron state [19]:

$$F_2^{2+}(2Mg) + e^- \quad \rightarrow \quad F_2^{+}(2Mg) \tag{3.1}$$

Fig. 3.3a illustrates the radiochromic transformation using the band structure of FNTDs. Both, the $F_2^{2+}(2Mg)$ centers as well as the $F_2^{+}(2Mg)$ centers produce fluorescence under optical excitation. The different absorption bands and the corresponding fluorescences are illustrated in Fig. 3.3b. $F_2^{2+}(2Mg)$ centers show absorption at 435 nm and produce green fluorescence with a wavelength of 510 nm. Contrary to this, $F_2^{+}(2Mg)$ centers posses absorption bands in the range of $260 - 620$ nm and produce red fluorescence with a wavelength of 750 nm [18]. The luminescence lifetime of both the $F_2^{2+}(2Mg)$ centers (9 ns) and the $F_2^{+}(2Mg)$ centers (75 ns) is short [17]. Indeed, there is also the possibility of a transformation without the influence of ionizing radiation. During crystal growth some $F_2^{2+}(2Mg)$ undergo a pre-transformation and result in measurable background signals. Since the number of pre-transformations could be dependent on the colorization, i.e. the sensitivity of the detectors, the background signal might be used to quantify the sensitivity of FNTDs. Prior background measurements of the detectors used in this thesis (cf. Fig C.1 and Fig. C.2) show partially high variations in the background signal within the detectors.

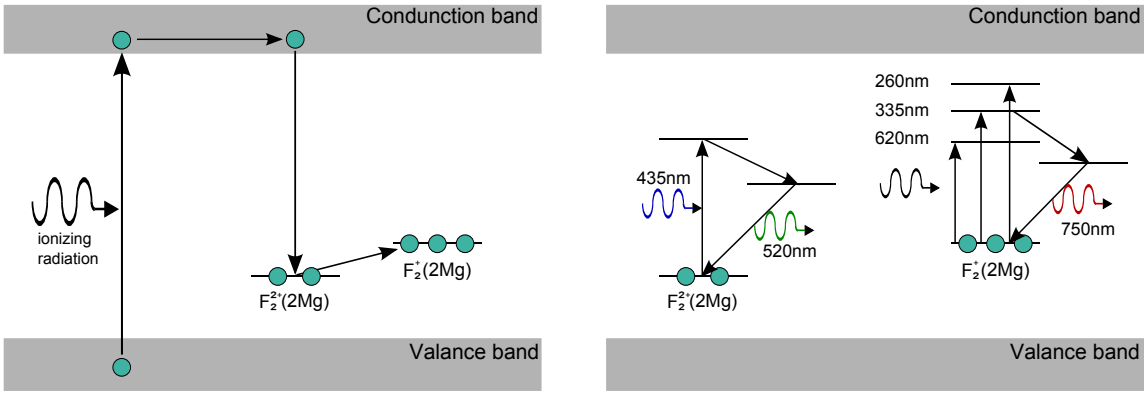

(a) Radiochromic transformation **(b)** Absorption bands

Figure 3.3 – Schematic illustration of the radiochromic transformation (a) and the different fluorescence properties of the $F_2^{2+}(2Mg)$ and $F_2^{+}(2Mg)$ centers (b) using the band structure of FNTDs. Ionizing radiation produces free electrons in the conduction band of the detector. Those electrons can be trapped by $F_2^{2+}(2Mg)$ centers and results due to radiochromic transformations in three electron states $F_2^{+}(2Mg)$. The fluorescence properties of F centers are dependent on the number of electrons trapped in one color center. Reproduced according to [15, 17].

3.1.3 Confocal microscopy based read out

The read out of the detectors is based on non-destructive laser induced fluorescence. Therefore, a confocal microscope can be used. The difference in the absorption bands allows to excite only the transformed F_2^+(2Mg) centers. Hence, bright visible track spots surrounded by dark background signal were detected [4]. Since the microscope excitation is not point-like, a small volume with lateral and axial spread is illuminated. Due to this axial spread, the measured intensity of a track spot corresponds to the mean energy loss of the particle along a small part of its track. The lateral spread leads to an averaged quantification of the local energy depositions. In this thesis, measuring the maximum signal of the track spots turned out to be a robust method for the fluorescence signal quantification. The short lifetime of luminescence results in time efficient read out due to fast laser scanning.

3.2 Zeiss LSM 710

The Zeiss LSM 710 confocal laser scanning microscope is part of the light microscopy facility at DKFZ. Different to conventional light microscopes, not the entire specimen is exposed but rather only a small part of it. This requires to perform a raster scan, to obtain a complete image of the specimen. Thus, the successive measured intensities, caused either by reflection or by fluorescence, are assembled after the read out and form the resulting image [20].

Fig. 3.4 illustrates the light path inside the LSM710 schematically. The light from different available laser sources passes trough a collimator and is then reflected by a dichroic beam splitter towards the specimen. The position of the objective determines the axial position z (read out depth) within the specimen where the laser beam is focused. The plane with this specific z is called focal plane. The settings of the scanning mirrors enable to modify the lateral x and y position of the focus point within the focal plane. Thus they are utilized to perform the raster scan of the specimen in a specific depth z [22].

The focused laser beam produces fluorescence light with a larger wavelength at the focus point. Since the dichroic beam splitter is permeable for those larger wavelengths and reflects only the initial laser light, the produced fluorescence light pass through the beam splitter and a second objective and is then detected with avalanche photo-diodes (APDs). The confocal pinhole right in front of the detector ensures that only fluorescence originating from a small slice around the focal plane reaches the detector [22].
Hence, the LSM710 suits well for FNTD read out. Since the fluorescence of F_2^+ color centers has to be induced to read out the detectors, a helium-neon laser with a wavelength of 633 nm was utilized (Sec. 3.3b).
The ZEN control software for the LSM710 was provided by the DKFZ's light microscopy facility and enables to control all read out parameters. Essential scanning parameters for the read out of FNTDs are listed in Tab. 3.1. The axial read out depth z and the

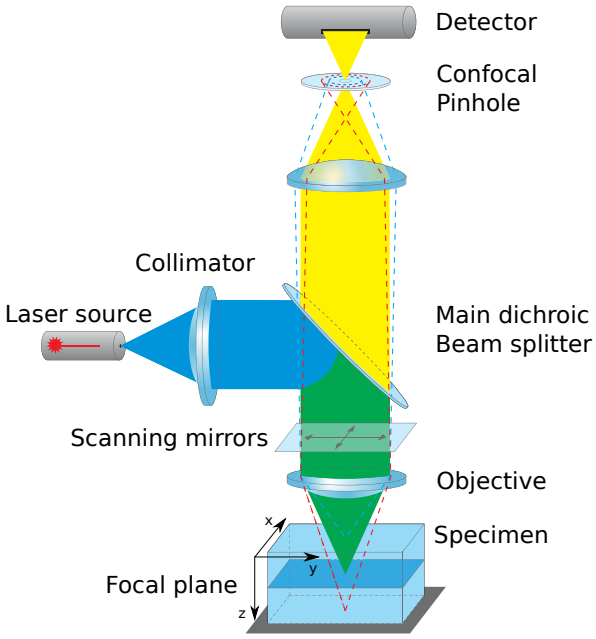

Figure 3.4 – Schematic illustration of the light path in the LSM710. The light of the laser source is reflected by the dichroic beam splitter towards the specimen. The settings of the scanning mirrors and the objective effect the lateral (x, y) and the axial z position of the beam focus. The fluorescence light, induced due to the focused laser beam, is able to pass through the dichroic beam splitter and is then detected with APDs. The diameter of the confocal pinhole limits the axial resolution of the read out. Reprinted from [21].

lateral (x, y)-position was adjusted using an external control unit.

Table 3.1 – Essential parameters for the read out of FNTDs using the LSM710 [22].

control parameters	**specification**
p	relative laser power
R	number of rescans
τ	dwell time for a single spot position
d_{pinhole}	pinhole diameter
g,Δg	change gray scale within ZEN
frame size	define the pixel resolution
image size	define the size of the image
bit depth	colour depth of the image

3.3 Software

3.3.1 Image processing

The images obtained from the confocal microscope were processed with ImageJ (version 1.47v), a free Java image processing program developed by Wayne Rasband [23]. For the determination of the single track spot positions and to obtain background images, the MOSAIC plug-ins *particle tracker* and *background subtractor*, developed at the Max-Planck-Institute Dresden, were used. The *particle tracker* function requires the approximate radius r of the tracks spots, a cut-off value C for the non-particle discrimination and a percentile P that determines which bright pixels are accepted as particles to identify the position of the single track spots. The *background subtractor* utilizes a sliding window with edge length a to determine the background intensities within the images. A more detailed description of those two plug-ins is given by S. Hoof [24].

3.3.2 Data evaluation

All further data evaluation was performed in R, a language and environment for statistical computing and graphics [25], using the not published package "FNTD" developed by S. Greilich et al. (DKFZ, Heidelberg). The calculation of LET values is based on tabulated SRIM data [26].

3.4 Heidelberg Ion-Beam Therapy Center

The Heidelberg Ion-Beam Therapy Center (HIT) is a clinical radiotherapy treatment facility. Since start-up in November 2009, patients were treated in three treatment rooms with protons and carbon ions. Besides radiotherapy treatment rooms, there is also the possibility to perform scientific experiments in a separated irradiation room. In addition to protons (^{1}H), also helium, carbon, and oxygen ions (^{4}He,^{12}C,^{16}O) are available for irradiations. A synchrotron with a preceding linear accelerator is used to create the required particle beams. Since HIT is primarily a clinical therapy center, the available energies of the different ion types correspond to water equivalent ranges of $2 - 31\,\mathrm{cm}$. This results in the following energy ranges in $\frac{\mathrm{MeV}}{\mathrm{u}}$ for the different ions:

$$1\mathrm{H} : (48.12 - 221.06) \tag{3.2}$$
$$4\mathrm{He} : (50.57 - 220.51) \tag{3.3}$$
$$12\mathrm{C} : (88.83 - 430.10) \tag{3.4}$$
$$16\mathrm{O} : (103.77 - 514.82) \tag{3.5}$$

Within these ranges, 255 energy increments are available for the irradiation with monoenergetic beams.

3.5 Data generation

3.5.1 Planing of the irradiations at HIT

The basis of analysis in this thesis is a set of 66 detectors irradiated with four different particles of various energies. To maximize the LET range of those irradiations, all available ion types at HIT (^{1}H,^{4}He,^{12}C,^{16}O) were included in the irradiation planning. The maximum possible LET range in Al_2O_3 from 1 $\frac{\text{keV}}{\mu\text{m}}$ to 150 $\frac{\text{keV}}{\mu\text{m}}$ is caused by the design and settings of the accelerator (cf. Sec. 3.4) and the requirement to measure in the entrance channel, i.e. using mono-energetic beams without fragments. This leads also to a LET gap between 13 $\frac{\text{keV}}{\mu\text{m}}$ and 34 $\frac{\text{keV}}{\mu\text{m}}$ due to inaccessible energies.
The linear as well as the logarithm scale was taken into account during planning the irradiations. The distances between the single data points were set in a way that the LET range is covered as uniformly as possible. The LET distribution of the planed irradiations, consisting of 22 data points, is illustrated in Fig. 3.5. The figure also indicates the use of the different ion types concerning the corresponding LET range.

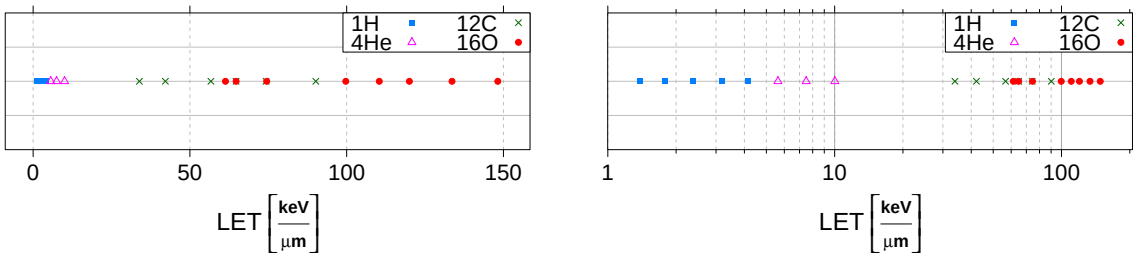

Figure 3.5 – Illustration of the the LET distribution of the data points in the linear (left) and in the logarithm (right) scale. Since only particle energies corresponding to clinical ranges are available, different LET ranges are covered from different ion types. The indicated LETs refer to the linear energy transfer in Al_2O_3.

To compensate for variability in colorization, three detectors for each LET were irradiated in the same irradiation cycle. To ensure homogeneous irradiations of all three detectors a fluence field with a size of $5 \times 5\,\text{cm}^2$ was chosen.

3.5.2 Experimental set-up and performed irradiations

All detectors were irradiated at HIT using the same experimental set-up shown in Fig. 3.6. In order to position the detectors precisely and perpendicularly to the beam line, they were attached to a PMMA block. This enables also to position the FNTDs at iso-center. All detectors were irradiated perpendicularly with the polished surface pointing towards the incident particles. Tab. A.1 summarizes all performed irradiations.

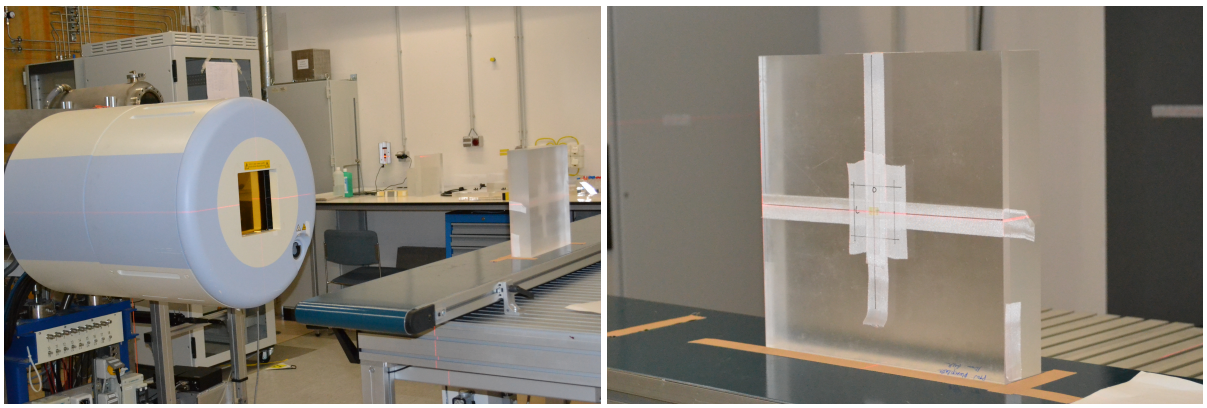

Figure 3.6 – Experimental set-up of irradiations at HIT (left) and the PMMA block with the attached FNTDs (right). The PMMA block enables to position the FNTDs accurate to the beam line and to ensure perpendicular irradiations.

3.5.3 Detector read out

To create a data set with data points which are as comparable as possible, most read out parameters were kept constant for every performed read out. This was easy to perform in the case of z, τ and R. Contrary to those parameters the relative laser power p has to be adapted for every LET level due to the saturation effects of the APDs [27]. Thus, the laser power was adjusted to ensure that the detected signal lies in the range of 2.5 MHz. Since prior background measurements result in a high intra-image variability (cf. Fig. C.1 and Fig. C.2), the irradiated detectors were read out on four different positions using the confocal microscope LSM710 (cf. Sec. 3.2). The essential read out parameters are given in Tab. B.1 and Tab. B.2. Fig. 3.7 shows an exemplary microscope image with bright visible track spots surrounded by dark background signal.
In order to position the FNTDs precise above the objective of the microscope, the detectors were placed on glass bottom micro-well dishes from MatTek Corp. (Ahland, Massachuesetts, USA). To minimize the refraction between different transmission media, thus to reduce the lateral spread of the laser beam, immersion oil between dish and objective as well as between dish and detector was utilized.

3.5.4 Determination of fluorescence track intensity

The images received from the read out with the confocal microscope consists of detected counts N caused by the fluorescence signals. Using the detected counts in combination with the dwell time τ and the number of rescans R enables to determine the detected count rate η_{detected} [27]:

$$\eta_{\text{detected}} = \frac{N}{R \cdot \tau} \tag{3.6}$$

In order to correct the detected count rate η_{detected} for the saturation of the APDs, the following inverse saturation function with an average saturation rate of $\eta_0 = 16.2\,\text{MHz}$

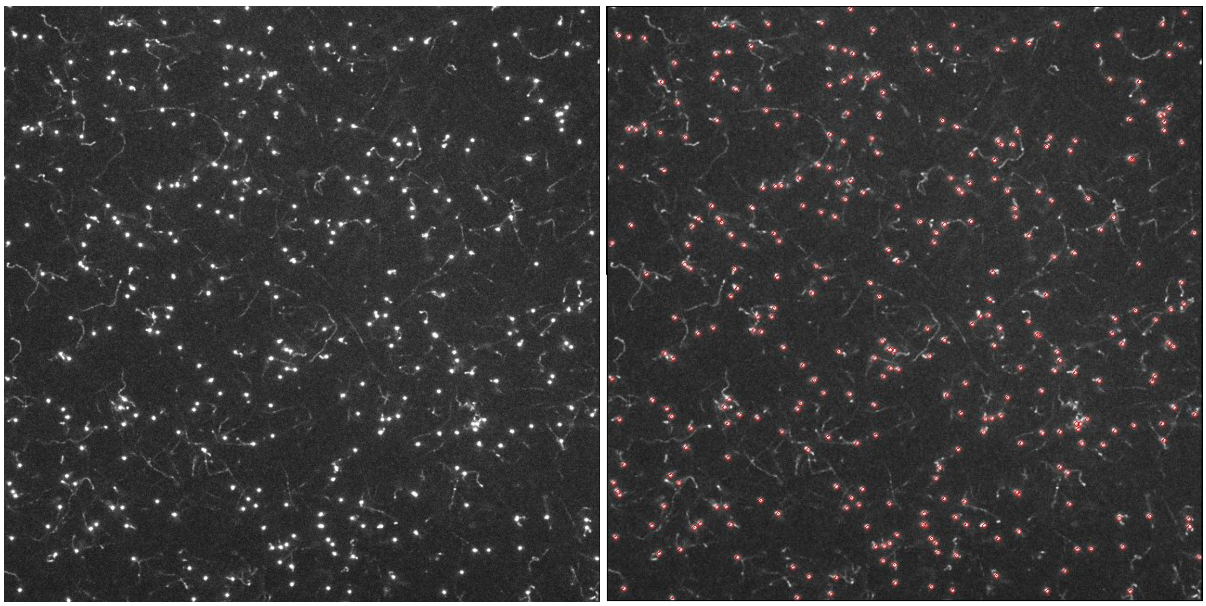

Figure 3.7 – Exemplary microscope image (raw data (left), with particle detection (right)) with size $134.8 \times 134.8\,\mu\text{m}^2$ of a FNTD irradiated with 281.57 $\frac{\text{MeV}}{\text{u}}$ carbon ions corresponding to a LET of 42.18 $\frac{\text{keV}}{\mu\text{m}}$. The read out was performed with full laser power $p = 100\%$ and a dwell time $\tau = 40.34\mu\text{s}$. Due to transformed color centers, caused by the energy deposition of the traversing particles, about 300 bright visible track spots surrounded by dark background signals were detected. The red circles around most of the track spots in the left image illustrate the result of the detection with the *particle tracker*.

is applied [27]:

$$\eta_{\text{actual}} = -\eta_0 \cdot \ln\left(1 - \frac{\eta_{\text{detected}}}{\eta_0}\right) \tag{3.7}$$

The position of each single track spot within an image was determined by using the *particle tracker* (Sec. 3.3). For this thesis, values of $r = 3$, $C = 3$ and $P = 0.1$ have turned out to be robust settings for the correct determination of the track spot position. It is of particular importance that no high energy electrons (δ-electrons) were wrongly detected as particles. An exemplary result of the *particle tracker* function is shown in Fig. 3.7. Using the single track positions enables to quantify the corresponding track signals.

As a proxy for the single track intensity the maximum actual count rate $\hat{\eta}_{\text{track,actual}}$ of a track spot was chosen. To determine the net track intensity η_{track}, the maximum actual count rate has to be corrected for the background signal $\eta_{\text{track,background}}$. The background intensities were determined by using the *background subtractor* (Sec. 3.3) with a edge length of $a = 5\,\text{pixel}$ and the corresponding track position:

$$\eta_{\text{track}} = \hat{\eta}_{\text{track,actual}} - \eta_{\text{track,background}} \tag{3.8}$$

In order to compare track intensities corresponding to read outs with different laser powers, net track intensities η_{track} were normalized to the laser power p [27] and a

correction factor f_{lp} [28] was applied:

$$\eta = \frac{\eta_{\mathrm{track}}}{p} f_{\mathrm{lp}} \quad \text{with} \quad f_{\mathrm{lp}} = \left(\frac{p_1}{p_2}\right)^{-0.164} \tag{3.9}$$

Talking about measured intensities concerns in the following to the adjusted count rates described in Eq. (3.9). We introduce an indexing system, where l designate the LET level consisting of $L = 22$ different levels, k indicates the detector with $K_l = 3$ detectors per LET level, j describes the read out position with $J_{kl} = 4$ different positions within each detector and i denotes the detected track within one microscope image with total number of approximately $I_{jkl} \approx 300$ per image. This results in a total number of about $80,000$ measured tracks. In fact this number rises, since results from different read outs of the same detectors were used for the analysis.

4 Experiments and Results

Since already observed LET-fluorescence relations suffer, especially in the clinical LET range, from large variabilities in the measured fluorescence signal [5], the data set received from the read out with the confocal microscope (cf. Tab. B.2) was analyzed in the following from several different angles. As prior background measurements (cf. App. C) result in some cases in high intra- and inter-detector fluctuations, the influence of such variabilities is investigated in the following. In addition, also microscope related variations were analyzed. The single track intensities η_{ijkl} measured in every image formed the basis of all following investigations. Variabilities in the energy of the incident particles were ignored, since the accelerator at HIT has a very high precision with negligible uncertainty concerning the mean energy and energy spread of the accelerated particles. The following influential factors were investigated:

- microscope related variability
  - read outs with different laser powers (Sec. 4.1.1)
  - read outs on different days (Sec. 4.1.2)
- detector related variability
  - intra-image fluctuations (Sec. 4.2.1)
  - intra-detector fluctuations (Sec. 4.2.2)
  - inter-detector fluctuations (Sec. 4.2.3)

All significance tests were performed on the condition of a 5% significance level.

4.1 Microscope related variability

To investigate fluctuations of the measured track intensities related to the read out with the confocal microscope, the track intensities depending on different laser powers and different read out days were analyzed. Since it is nearly impossible to identify two measured track intensities η_{ijkl} in different images with the same particle track, the mean track intensities in one image μ_{jkl} were used:

$$\mu_{jkl} = \frac{1}{I_{jkl}} \sum_{i=1}^{I_{jkl}} \eta_{ijkl} \tag{4.1}$$

They were easy to compare with each other since all necessary information such as LET, detector id and the read out position were well documented in the image name.

4.1.1 Laser power

To analyze the influence of different laser powers, and to check if the normalization to the laser power and the applied correction factor f_{lp} is feasible, the results of the second read out cycle (cf. Tab. B.2) were utilized. Therefore the intensities obtained from read outs with variable laser powers $\mu_{jkl,\mathrm{lpany}}$ are plotted in Fig. 4.1 against the corresponding intensities $\mu_{jkl,\mathrm{lp100}}$ received from full laser power read out of the same detectors. Both read outs were performed shortly after each other, to exclude time dependent fluctuations of the microscope.

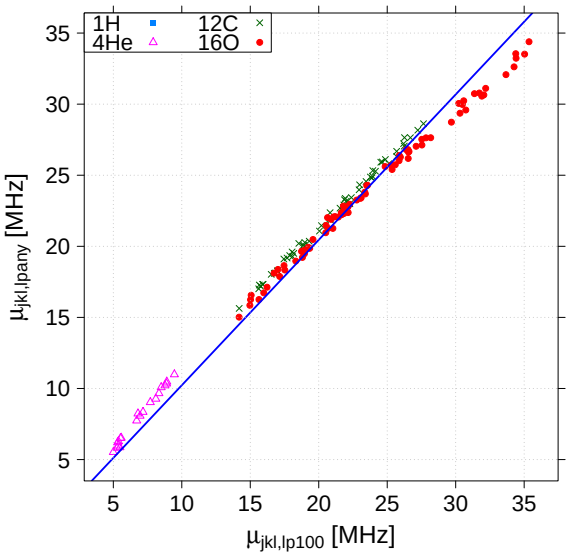

Figure 4.1 – Comparison of the resulting intensities obtained from the read out with variable laser power $\mu_{jkl,\mathrm{lpany}}$ and from the read out with full laser power $\mu_{jkl,\mathrm{lp100}}$ of the same detectors. Intensities resulting from irradiations with different ion types are indicated with varied plot symbols. The data points were fitted with a linear model of the type: $\mu_{jkl,\mathrm{lpany}} = m_1 \cdot \mu_{jkl,\mathrm{lp100}}$ with the result: $m_{1,\mathrm{fit}} = (1.023 \pm 0.004)$.

If there would be no difference between the read out with constant full laser power and the read out with variable laser powers, the points in Fig. 4.1 would fall on a line with a slope of $m_{\mathrm{ideal}} = 1$. Hence the data points were fitted with a linear model:

$$\mu_{jkl,\mathrm{lpany}} = m_1 \cdot \mu_{jkl,\mathrm{lp100}} \quad \text{with} \quad m_{1,\mathrm{fit}} = (1.023 \pm 0.004) \tag{4.2}$$

The resulting slope $m_{1,\mathrm{fit}}$ is close to m_{ideal}, nonetheless it still deviates significantly ($p = 1.29 \cdot 10^{-10}$).

When all measured intensities μ_{jkl} are tested on linear dependencies, both LET and laser power are significant:

$$\mu_{jkl} \propto \mathrm{LET} + \mathrm{lp} \tag{4.3}$$

$$p_{\mathrm{LET}} < 2 \cdot 10^{-16} \quad , \quad p_{\mathrm{lp}} = 6.25 \cdot 10^{-6} \tag{4.4}$$

4.1.2 Time dependent microscope influences

In order to analyze if there is a day-to-day variability of the microscope, the results of the first and the second read out of the oxygen range (cf. Tab. B.2) were utilized. Analogical to the previous section the measured intensities $\mu_{jkl,1\mathrm{st}}$ and $\mu_{jkl,2\mathrm{nd}}$ are plotted against each other in Fig. 4.2 and a linear fit is applied:

$$\mu_{jkl,1\mathrm{st}} = m_2 \cdot \mu_{jkl,2\mathrm{nd}} \quad \text{with} \quad m_{2,\mathrm{fit}} = (1.025 \pm 0.008) \tag{4.5}$$

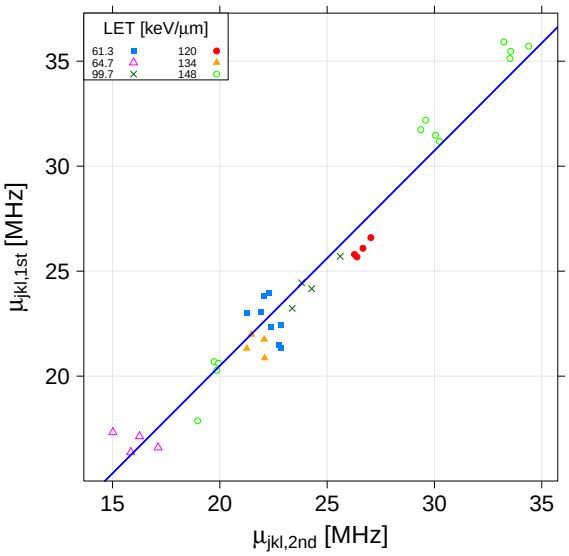

Figure 4.2 – Comparison of the resulting intensities obtained from the first read out cycle $\mu_{jkl,1\mathrm{st}}$ and of the second read out cycle $\mu_{jkl,2\mathrm{nd}}$ concerning detectors in the oxygen range. Intensities resulting from irradiations with different LETs are indicated with varied plot symbols. The data points were fitted with a linear model of the type: $\mu_{jkl,1\mathrm{st}} = m_2 \cdot \mu_{jkl,2\mathrm{nd}}$ with the result: $m_{2,\mathrm{fit}} = (1.025 \pm 0.008)$.

Also $m_{2,\mathrm{fit}}$ deviates slightly but significantly from m_{ideal} ($p = 0.003$). When μ_{jkl} was tested analogically to the previous section on different linear dependencies, only the LET is significant:

$$\mu_{jkl} \propto \mathrm{LET} + \mathrm{lp} + \text{read out} \tag{4.6}$$

$$p_{\mathrm{LET}} = 9.08 \cdot 10^{-5} \quad , \quad p_{\mathrm{lp}} = 0.074 \quad , \quad p_{\text{read out}} = 0.186 \tag{4.7}$$

4.2 Detector related variability

Besides the read out with the confocal microscope, the detector itself represents a possible source of uncertainty. To investigate detector related variabilities, the fluctuations of the measured fluorescent signals within an image, a detector and one LET level (three different detectors) were investigated. Therefore the results of the second read out cycle (cf. Tab. B.2) were utilized.

As described in Sec. 3.5.4, L indicates the number of different LET levels, K_l specifies the number of detectors corresponding to a LET level, J_{kl} describes the number of different read out positions within each detector and I_{jkl} denotes the number of detected tracks within the corresponding image. The uncapitalized letters l, k, j and i are the corresponding indices.

4.2.1 Intra-image fluctuations

We assume the detector influence to be small within a single image and that all variability is caused by fluctuations in the energy loss of the traversing particles. All detected track signals η_{ijkl} within one image were averaged. The corresponding standard deviation σ_{jkl} is a measure for the intra-image fluctuation of the intensities and should, therefore, be a measure for the variability in the energy loss:

$$\sigma^2_{\epsilon,jkl} = \frac{1}{I_{jkl}-1}\sum_{i=1}^{I_{jkl}}\left(\eta_{ijkl}-\mu_{jkl}\right)^2 \quad \text{with} \quad \mu_{jkl} = \frac{1}{I_{jkl}}\sum_{i=1}^{I_{jkl}}\eta_{ijkl} \tag{4.8}$$

The index ϵ indicates that $\sigma_{\epsilon,jkl}$ is caused by fluctuations in the energy loss of the particle. The corresponding physical process is the relative energy loss straggling. The standard deviations were divided by μ_{jkl} to obtain the relative intra-image fluctuations:

$$\hat{\sigma}_{\epsilon,jkl} = \frac{\sigma_{\epsilon,jkl}}{\mu_{jkl}} \tag{4.9}$$

To investigate, if $\hat{\sigma}_{\epsilon,jkl}$ differs for different LET l, different detectors k or for different read out positions j on the detector, the relative standard deviations were tested on significant dependencies:

$$\hat{\sigma}_{\epsilon,jkl} \propto l + k + j \tag{4.10}$$

$$p_l < 2 \cdot 10^{-16} \quad , \quad p_k = 0.148 \quad , \quad p_j = 0.938 \tag{4.11}$$

The resulting p-values show that the relative intra-image fluctuation is only significantly dependent on the LET level l (cf. Fig. 4.3). Hence, $\sigma_{\epsilon,jkl}$ can be averaged over all positions J_{kl} and all detectors K_l:

$$\hat{\sigma}_{\epsilon,l} = \langle\hat{\sigma}_{\epsilon,jkl}\rangle_{jk} = \frac{1}{K_l}\sum_{k=1}^{K_l}\frac{1}{J_{kl}}\sum_{j=1}^{J_{kl}}\hat{\sigma}_{\epsilon,jkl} \tag{4.12}$$

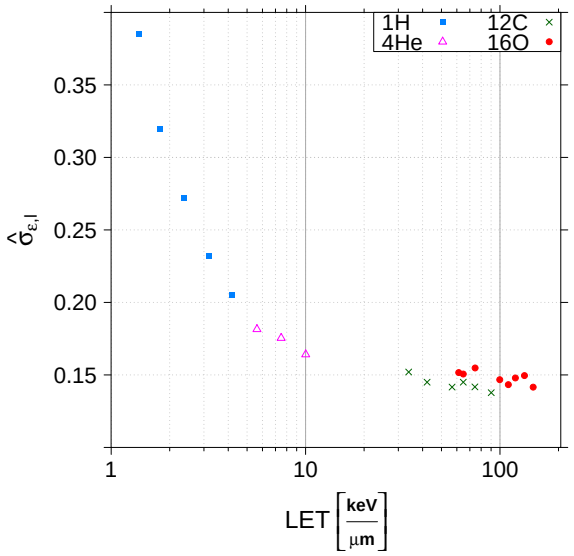

Figure 4.3 – Relative intra-image fluctuations $\hat{\sigma}_{\epsilon,l}$ in the measured fluorescence signal as a function of the LET in Al_2O_3 in a lin-log plot. Intensity fluctuations regarding irradiations with different ion types are indicated with varied plot symbols. For low LETs $\hat{\sigma}_{\epsilon,l}$ lies up to 35%. Already in the helium range $\hat{\sigma}_{\epsilon,l}$ reduces to about 16% and levels of at 14% in higher LET ranges. The corresponding physical quantity is the relative energy loss straggling of the particles traversing through the detector.

Fig. 4.3 illustrates the mean relative energy straggling $\hat{\sigma}_{\epsilon,l}$ in dependence of the LET and shows a strong dependency. In the range of irradiations with protons and helium the variability decreases strongly with rising LET. Only in the higher LET range, corresponding to carbon and oxygen irradiations, the fluctuations are almost constant. Commencing with a relative straggling of more than 35% the fluctuations already reduce in the helium range to a value of about 16%. In the LET range from 30 $\frac{\text{keV}}{\mu\text{m}}$ to 150 $\frac{\text{keV}}{\mu\text{m}}$ the relative energy loss straggling levels off at a value of about 14%. This result corresponds to the observed stochastic energy deposition along individual ion trajectories (G. Klimpki, Master's thesis 2014).

4.2.2 Intra-detector fluctuations

To quantify intra-detector variabilities, the mean image intensities μ_{jkl} within one detector were averaged and the corresponding standard deviation σ_{kl} was determined:

$$\sigma_{kl}^2 = \frac{1}{J_{kl}-1}\sum_{j=1}^{J_{kl}}(\mu_{jkl}-\mu_{kl})^2 \quad \text{with} \quad \mu_{kl} = \frac{1}{J_{kl}}\sum_{j=1}^{J_{kl}}\mu_{jkl} \tag{4.13}$$

Analogically to the previous section, σ_{kl} is a measure for the intra-detector fluctuation which is a result of fluctuations caused by different read out positions as well as a consequence of intra-image variabilities. Hence, to isolate the variability resulting only from

different read out positions $\sigma_{\mathrm{P},kl}$, the uncertainties $\mathrm{u}_{\epsilon,l}$ caused by intra-image fluctuations have to be considered[1]:

$$\sigma^2_{\mathrm{P},kl} = \sigma^2_{kl} - \mathrm{u}^2_{\epsilon,l} \quad \text{with} \quad \mathrm{u}_{\epsilon,l} = \frac{\hat{\sigma}_{\epsilon,l} \cdot \mu_{kl}}{\sqrt{\langle I_{jkl} \rangle_{jk}}} \tag{4.14}$$

Fig. 4.4 shows the ratio of σ_{kl} and $\mathrm{u}_{\epsilon,l}$ in dependence on the LET. Since the average ratio is larger than 4, corresponding to a $\mathrm{u}^2_{\epsilon,l}$-influence of about 6%, the influence of $\mathrm{u}_{\epsilon,l}$ can be neglected:

$$\sigma_{\mathrm{P},kl} \approx \sigma_{kl} \quad \text{with} \quad \hat{\sigma}_{\mathrm{P},kl} = \frac{\sigma_{\mathrm{P},kl}}{\mu_{kl}} \tag{4.15}$$

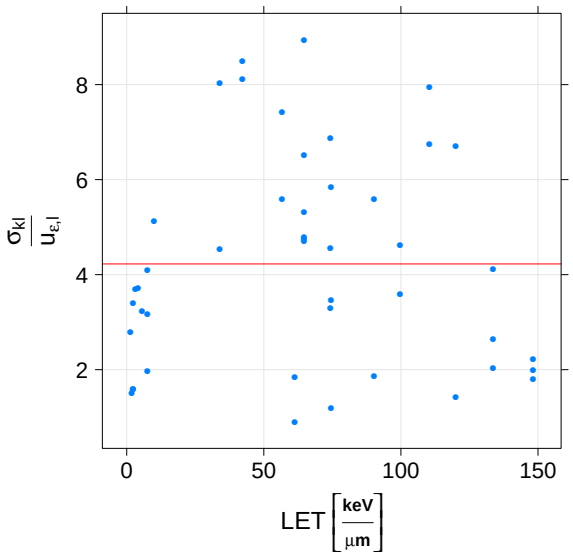

Figure 4.4 – Comparison of intra-detector fluctuations σ_{kl} and the uncertainties caused by intra-image fluctuations $\mathrm{u}_{\epsilon,l}$ using the ratio $\sigma_{kl}/\mathrm{u}_{\epsilon,l}$ in dependence of the LET in Al_2O_3. Since the averaged ratio lies up to a value of 4, corresponding to a $\mathrm{u}^2_{\epsilon,l}$-influence of about 6%, the influence of $\mathrm{u}_{\epsilon,l}$ is negligible small.

To check if $\hat{\sigma}_{\mathrm{P},kl}$ is dependent on the LET level l or the detector k, the position variabilities were tested on significant correlations:

$$\hat{\sigma}_{\mathrm{P},kl} \propto l + k \tag{4.16}$$

$$p_l = 0.060 \quad , \quad p_k = 0.628 \tag{4.17}$$

According to the p-values there is no significant dependence of $\hat{\sigma}_{\mathrm{P},kl}$ on different detectors k or on the LET level l. Therefore $\hat{\sigma}_{\mathrm{P},kl}$ was averaged over all detectors K_l and all LET

[1] $\langle \cdots \rangle_{jk}$ indicates averaging over all positions j and all detectors k

levels L. This results in a global relative influence of intra-detector fluctuations caused by different read out positions j, for the entire detector set:

$$\hat{\sigma}_{\mathrm{P}} = \langle \hat{\sigma}_{\mathrm{P},kl} \rangle_{kl} = \frac{1}{L} \sum_{l=1}^{L} \frac{1}{K_l} \sum_{k=1}^{K_l} \hat{\sigma}_{\mathrm{P},kl} \quad \text{with} \quad \mathrm{u}_{\hat{\sigma}_{\mathrm{P}}} = \frac{\sigma_{\hat{\sigma}_{\mathrm{P}}}}{\sqrt{L \cdot K_l}} \tag{4.18}$$

$$\boxed{\hat{\sigma}_{\mathrm{P}} = (4.0 \pm 0.3)\%} \tag{4.19}$$

4.2.3 Inter-detector fluctuations

Following the same procedure as in the previous sections, the mean detector intensities μ_{kl} were averaged within each LET level and the corresponding standard deviation was determined to quantify inter-detector fluctuations in the measured intensities:

$$\sigma_l^2 = \frac{1}{K_l - 1} \sum_{k=1}^{K_l} (\mu_{kl} - \mu_l)^2 \quad \text{with} \quad \mu_l = \frac{1}{K_l} \sum_{k=1}^{K_l} \mu_{kl} \tag{4.20}$$

σ_l is an indicator for the inter-detector variability which is a result of variabilities caused by different detector sensitivities as well as a consequence of intra-detector fluctuations. Analogically to the previous section, the uncertainties $\mathrm{u}_{\mathrm{P},l}$ have to be considered to isolate the variabilities $\sigma_{\mathrm{D},l}$ resulting only from the read out of different detectors:

$$\sigma_{\mathrm{D},l}^2 = \sigma_l^2 - \mathrm{u}_{P,l}^2 \quad \text{with} \quad \mathrm{u}_{\mathrm{P},l} = \frac{\hat{\sigma}_{\mathrm{P}} \cdot \mu_l}{\sqrt{\langle J_{kl} \rangle_k}} \tag{4.21}$$

Fig. 4.5 illustrates analogically to Fig. 4.4 the ratio of both uncertainties. The intra-detector influences are negligible since σ_l is on average more than eight times larger than $\mathrm{u}_{P,l}$, corresponding to a $\mathrm{u}_{P,l}^2$-influence of about 1.5%:

$$\sigma_{\mathrm{D},l} \approx \sigma_l \quad \text{with} \quad \hat{\sigma}_{\mathrm{D},l} = \frac{\sigma_{\mathrm{D},l}}{\mu_l} \tag{4.22}$$

In order to see if $\hat{\sigma}_{\mathrm{D},l}$ is dependent on different LET levels l, the relative variabilities were checked on significant LET influences:

$$\hat{\sigma}_{D,l} \propto l \qquad p_l = 0.772 \tag{4.23}$$

Since the result shows no significant dependency on the LET level l (high p_l), $\hat{\sigma}_{\mathrm{D},l}$ was averaged over all LET levels L^* [2], to obtain the global relative influence of inter-detector variabilities caused by different detectors k:

$$\hat{\sigma}_{\mathrm{D}} = \langle \hat{\sigma}_{\mathrm{D},l} \rangle_l = \frac{1}{L^*} \sum_{l=1}^{L^*} \hat{\sigma}_{\mathrm{D},l} \quad \text{with} \quad \mathrm{u}_{\hat{\sigma}_{\mathrm{D}}} = \frac{\hat{\sigma}_{\mathrm{D}}}{\sqrt{L^*}} \tag{4.24}$$

$$\boxed{\hat{\sigma}_D = (16.2 \pm 2.1)\%} \tag{4.25}$$

[2] L^* indicates the number of LET levels where more than one detector is read out and $K_l > 1$ is given

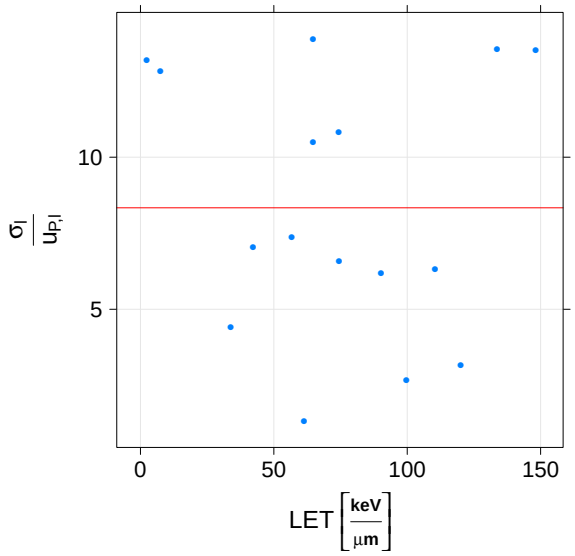

Figure 4.5 – Comparison of inter-detector fluctuations σ_l and the uncertainties caused by intra-detector fluctuations $u_{P,l}$ using the ratio $\sigma_l/u_{P,l}$ in dependence of the LET in Al_2O_3. Since the averaged ratio lies up to a value of 8, corresponding to a $u^2_{P,l}$-influence of about 1.5%, the influence of $u_{P,l}$ is negligible small.

4.3 LET-fluorescence relation

In order to obtain a final relation between LET and measured fluorescence signal, the mean measured intensities within one LET level μ_l were utilized:

$$\mu_l = \frac{1}{K_l}\sum_{k=1}^{K_l}\frac{1}{J_{kl}}\sum_{j=1}^{J_{kl}}\frac{1}{I_{jkl}}\sum_{i=1}^{I_{jkl}}\eta_{ijkl} \tag{4.26}$$

To determine the corresponding relative uncertainties $\hat{u}_l$, the propagation of each single source of uncertainty has to be considered, for which the results of Sec. 4.2 were employed. The determined relative variances $\hat{\sigma}^2_D$, $\hat{\sigma}^2_P$ and $\hat{\sigma}^2_{\epsilon,l}$ represent the best estimate for the actual variances and were, therefore, utilized to determine the corresponding standard error of the mean:

$$\hat{u}_l = \frac{1}{\mu_l}\sqrt{u^2_{inter-detector} + u^2_{intra-detector} + u^2_{intra-image}} \tag{4.27}$$

$$= \frac{1}{\mu_l}\sqrt{\frac{\hat{\sigma}^2_D\mu_l^2}{K_l} + \frac{1}{K_l^2}\sum_{k=1}^{K_l}\frac{\hat{\sigma}^2_P\mu^2_{kl}}{J_{kl}} + \frac{1}{K_l^2}\sum_{k=1}^{K_l}\frac{1}{J^2_{kl}}\sum_{j=1}^{J_{kl}}\frac{\hat{\sigma}^2_{\epsilon,l}\mu^2_{jkl}}{I_{jkl}}} \tag{4.28}$$

For the analysis of the data set in this thesis it is legitimate to make the assumptions:

$$J_{kl} = 4 \quad , \quad I_{jkl} \approx \langle I_{jkl}\rangle_{jk} \quad , \quad \mu_{kl} \approx \mu_{jkl} \approx \mu_l \tag{4.29}$$

Every detector was read out on four different read out positions j, thus J_{kl} can be replaced by four. Since every detector corresponding to the same LET level l was irradiated using the same particle fluence (cf. Tab. A.1), it is valid to replace the number of detected tracks in every image I_{jkl} by the mean detected tracks per image in one LET level l $\langle I_{jkl}\rangle_{jk}$. In addition the mean image intensities μ_{jkl} and mean detector intensities μ_{kl} were assumed to equal the mean LET intensities μ_l. Applying these assumptions simplifies the error estimation enormously:

$$\hat{\mathrm{u}}_l \approx \frac{1}{\mu_l}\sqrt{\frac{\hat{\sigma}_D^2\mu_l^2}{K_l} + \frac{\hat{\sigma}_P^2\mu_l^2}{4K_l} + \frac{\hat{\sigma}_{\epsilon,l}^2\mu_l^2}{4K_l\langle I_{jkl}\rangle_{jk}}} \tag{4.30}$$

$$= \frac{1}{\sqrt{K_l}}\sqrt{\hat{\sigma}_D^2 + \frac{\hat{\sigma}_P^2}{4} + \frac{\hat{\sigma}_{\epsilon,l}^2}{4\langle I_{jkl}\rangle_{jk}}} \tag{4.31}$$

Fig. 4.6 and 4.7 show the resulting correlation between LET and the measured fluorescence intensity in a double log plot, on the one hand for the LET in Al_2O_3 (cf. Fig. 4.6) and on the other hand for the LET in H_2O (cf. Fig. 4.7). The error bars indicate the standard uncertainty u_l. An exponential saturation function was fitted to the data points:

$$f(\mathrm{LET}) = A \cdot \left[1 - \exp\left(-\frac{\mathrm{LET}}{B}\right)\right] \tag{4.32}$$

$$\text{LET in } Al_2O_3 : A_{\text{fit}} = (25.1 \pm 0.8)\,\mathrm{MHz} \quad B_{\text{fit}} = (23.8 \pm 3.0)\,\frac{\mathrm{keV}}{\mu\mathrm{m}} \tag{4.33a}$$

$$\text{LET in } H_2O : A_{\text{fit}} = (25.1 \pm 0.8)\,\mathrm{MHz} \quad B_{\text{fit}} = (7.37 \pm 0.93)\,\frac{\mathrm{keV}}{\mu\mathrm{m}} \tag{4.33b}$$

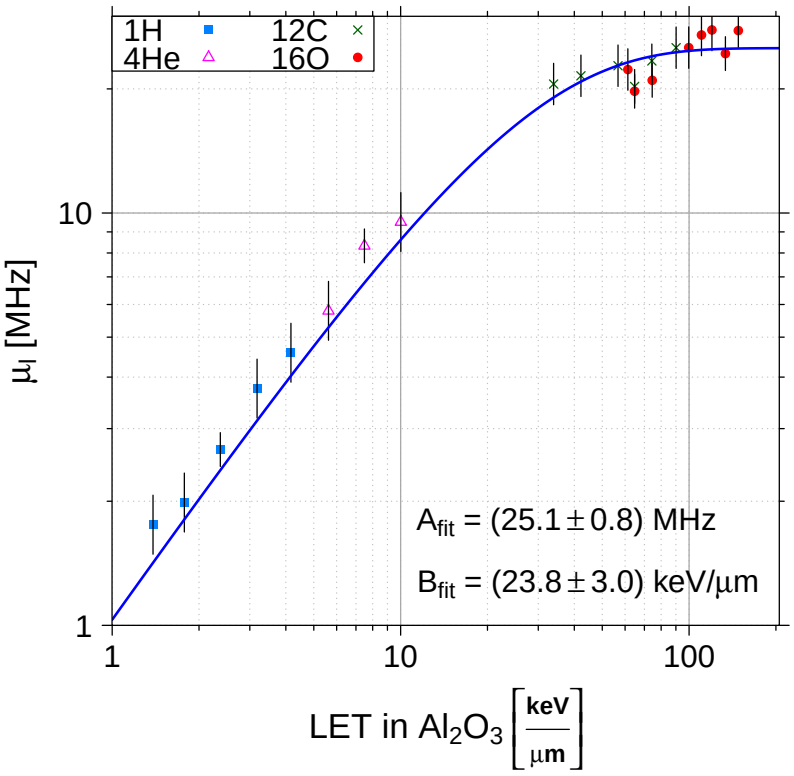

Figure 4.6 – Mean measured fluorescence signals within one LET level l in dependence of the LET in Al_2O_3 in a double log plot. Intensities resulting from irradiations with different ion types are indicated with varied plot symbols. The data points were fitted with a saturation function of the type: f(LET)=A(1-exp(-LET/B). The error in the fluorescence signal was determined according to Eq. 4.31.

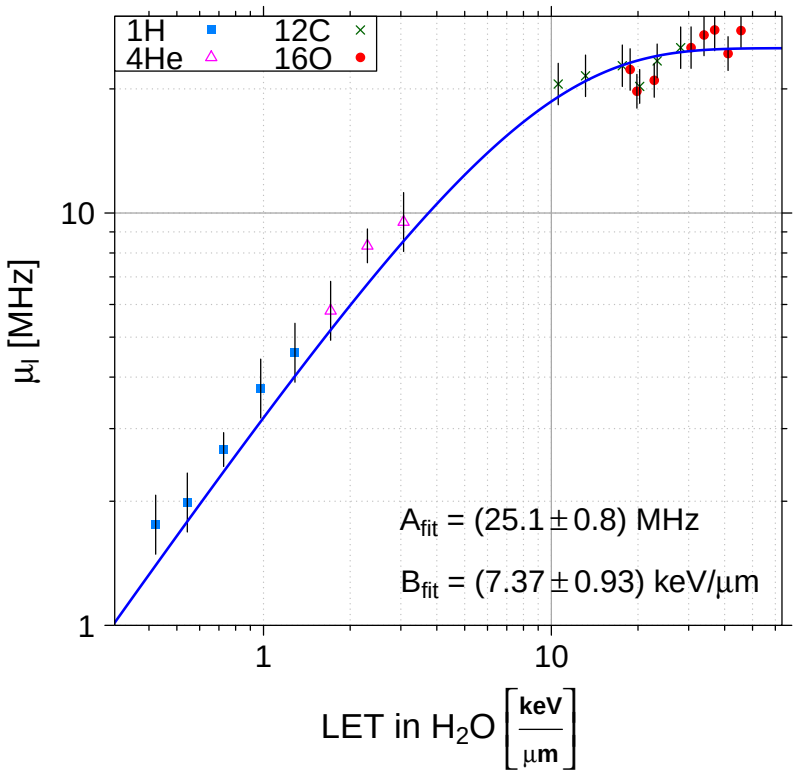

Figure 4.7 – Mean measured fluorescence signals within one LET level l in dependence of the LET in H_2O in a double log plot. Intensities resulting from irradiations with different ion types are indicated with varied plot symbols. The data points were fitted with a saturation function of the type: f(LET)=A(1-exp(-LET/B)). The error in the fluorescence signal was determined according to Eq. 4.31.

5 Discussion

5.1 Microscope influence

The comparison of read outs concerning same detectors performed on different read out days shows no significant time dependency (cf. p-values Sec. 4.1.2). Thus, fluctuations in the measured signals caused by time dependent variations on the part of the microscope are small and can be neglected.

Contrary to this, the analysis of read outs performed in quick succession but with different laser powers, on the one hand with a low laser power p_1 and the other hand with full laser power $p_2 = 100\%$, results in a significant p_{lp}-value (cf. Sec. 4.1.1). To isolate the different influences, the analyzed data set was divided regarding the utilized laser power p_1, and the significance dependencies were tested again. Since each detector corresponding to a specific ion type was read out with the same laser power p_1 (except for 4He), this leads also to a division concerning the different ion types:

$$\mu_{jkl} \propto \mathrm{LET} + \mathrm{lp} \quad \Rightarrow \quad p_{\mathrm{lp}} = 0.738 \quad (^{16}\mathrm{O}) \quad p_1 = 7\% \tag{5.1}$$

$$\mu_{jkl} \propto \mathrm{LET} + \mathrm{lp} \quad \Rightarrow \quad p_{\mathrm{lp}} = 0.057 \quad (^{12}\mathrm{C}) \quad p_1 = 10\% \tag{5.2}$$

$$\mu_{jkl} \propto \mathrm{LET} + \mathrm{lp} \quad \Rightarrow \quad p_{\mathrm{lp}} = 0.006 \quad (^{4}\mathrm{He}) \quad p_1 = 25\%, 60\% \tag{5.3}$$

According to the resulting p-values the influence of changing the laser power from p_1 to p_2 is dependent on the applied low laser power p_1. In the case of low p_1 in the oxygen range the resulting intensities do not differ significantly. Indeed, in the case of higher p_1 as in the carbon and in the helium range, the measured intensities of the different laser power read outs differ significantly.

Actually, the change of the laser power from p_1 to p_2 would have been corrected by applying the correction factor $f_{lp} = (p_1/p_2)^{-0.164}$ introduced in Sec. 3.5.4. The resulting p-values, however, indicate that f_{lp} does not seem to be universal. Thus the influence of different laser power or different ions is not fully understood, yet. However, since the slope of the linear fit in Fig. 4.1 differs only slightly from $m_{ideal} = 1$, the influence of different laser powers is negligibly small.

5.2 Detector influence

The investigations regarding detector related influences in the measured fluorescence signal show that the fluctuation within one LET level is dominated by inter-detector variabilities (cf. Sec. 4.2). Differences in the detection sensitivity represent one possible explanation for the large inter-detector fluctuations. One possible approach to quantify the sensitivity of the detectors is to analyze if there is a signal-to-background correlation. Therefore, the mean image intensities $\mu_{jkl,\text{track}}$ are plotted in Fig. 5.1 against the corresponding mean local background intensities $\mu_{jkl,\text{background}}$. It can be seen from the figure that the signal-to-background relation is potentially dependent on the utilized ion type. For oxygen and carbon the track intensity seems to be strongly dependent on the background signal whereas in the case of proton and helium irradiations the background signal seems to have no influence.

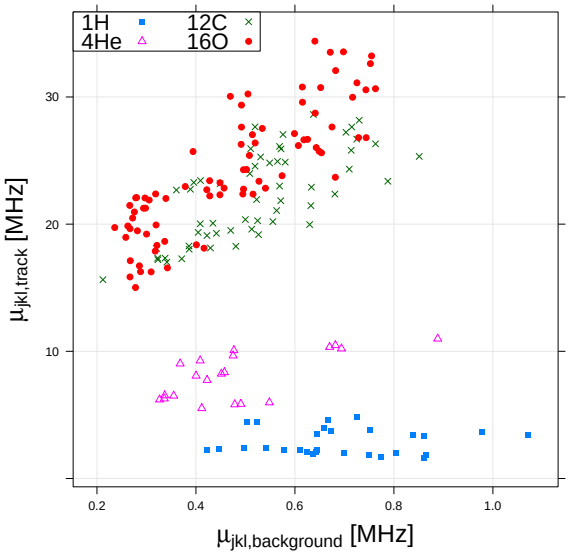

Figure 5.1 – Mean fluorescence track intensities in one image $\mu_{jkl,\text{track}}$ in dependence of the corresponding mean local background intensities $\mu_{jkl,\text{background}}$. Intensities resulting from irradiations with different ion types are indicated with varied plot symbols. The plot shows an ion specific behavior regarding the signal-to-background relation. Since in this data set ion specific also refers to LET specific and as a result the different measured intensities overlap only in the case of carbon and oxygen, no scientific verifiable statement can be provided concerning a signal-to-background correlation.

However, in the analyzed data set different ion types cover different LET ranges (cf. Sec. 3.5) and the measured intensities concerning different ion types overlap only in the case of carbon and oxygen. Thus, an ion specific behavior can also be a LET specific relation. Therefore, no scientific verifiable statement can be provided concerning a signal-to-background correlation. Furthermore, it would be of particular interest to investigate for example the signal-to-background relation for high LET proton irradiations.

Nevertheless, this potential ion or LET specific behavior might be the reason why a simple signal to background normalization is defective and leads to no better results concerning the inter-detector fluctuations.

Besides the magnitude of the variabilities, also its dependency on the LET level l, on the detector k and on the read out position j was investigated. The inter and intra detector fluctuations show no significant correlations whereas the intra image variabilities, corresponding to the relative energy loss straggling of a particle, results in a strong LET dependent course. The same behavior can be observed when measuring the stochastic energy deposition along individual ion trajectories (G. Klimpki, Master's thesis 2014). Since for higher LET irradiations particles with a higher nuclear charges Z_p were required, there might be also a dependence of the relative energy loss straggling to Z_p.

5.3 LET-curve

The mean measured intensities within one LET level l were used to establish a relation between those two quantities. The resulting correlation is described by a saturation function fitted to the data points of the kind $f(\mathrm{LET}) = A(1 - \exp(-\mathrm{LET}/B))$. This result is in contradiction to the already observed LET-fluorescence relation for higher LETs, since they measured no saturation even at an LET in H_2O of $8767\frac{\mathrm{keV}}{\mu\mathrm{m}}$ [4]. As the measured intensities were adjusted concerning the saturation of the APDs, this can not be the reason for the observed saturation course. Using the track maximum as an estimator for the track intensities might be not appropriate. However, similar evaluation of the measured data using the results of a gaussian fit instead of the track maximum lead also to a saturation curse. A possible explanation for different results in the observed relation is the fact, that for this study special, noise-reduced FNTDs were used.

The observed correlation in Fig. 5.3 is a result of a variety of intensity measurements, meaning that for one LET data point up to $7,000$ track intensities η_{ijkl} were averaged. The aim is to use such a relation between LET and measured fluorescence signal to determine the LET of a single particle by measuring its fluorescence track signal η_{ijkl}. Mathematically, the LET itself is easy to determine using the inverse of the observed relation (cf. App. D):

$$\eta_{ijkl} = f(\mathrm{LET}, \Phi_n) \qquad \Rightarrow \quad \mathrm{LET}^* = f^{-1}(\eta_{ijkl}*, \Phi_n) \tag{5.4}$$

where $f(\mathrm{LET}, \Phi_n)$ is the observed functional relation with parameters Φ_n, and LET* is the LET corresponding to the measured track signal $\eta_{ijkl}*$.

The uncertainty of this determination is of particular interest. There are a lot of different approaches to calculate the LET confidence interval of such an inverse problem. The three major approaches are the Delta-Method, the Wald-Method and the Bootstrapping method. All three approaches have been implemented into the statistic program R in an internship prior to this Bachelor's thesis. Background and theory information can be found in the final report (cf. App. D).

6 Conclusion and Outlook

6.1 Conclusion

The aim of this Bachelor's thesis was to identify and potentially quantify the major sources of variability concerning the measured fluorescence signals. Variabilities in the energy of the incident particles due to fluctuations in the acceleration process at HIT have been ignored, since this leads to small uncertainties compared to the investigated sources of variability.

While the influence of microscope related variabilities such as different read out days and the read out with different laser powers is small and can be neglected (cf. Sec. 5.1), detector related fluctuations represent the major source of uncertainty. Relative intra-image fluctuations $\hat{\sigma}_{\epsilon,l}$, related to the relative energy loss straggling, show a strong LET dependent course and lie in the range of $14 - 38\%$ (cf. Sec. 4.2.1). Contrary to this, intra-detector and inter-detector fluctuations show no significant dependence neither concerning the LET level l, the detector k nor the read out position j. They lie in the magnitude of $\hat{\sigma}_D \approx 16\%$ in the inter-detector case (cf. Sec. 4.2.3) and $\hat{\sigma}_P \approx 4\%$ in the intra-detector case (cf. Sec. 4.2.2). Due to the propagation of the single uncertainties (cf. Sec. 5.3), the total uncertainty of the mean LET intensities μ_l, required for a LET-fluorescence relation, is, indeed, dominated by inter-detector fluctuations.

The determined relation between LET and the measured mean fluorescence intensities μ_l shows a saturation course. Due to the large dependency on inter-detector fluctuations this calibration might not exhibit the required precision for an accurate determination of the LET by using measured fluorescence track signals, but represents the first calibration curve concerning the clinical LET range.

6.2 Outlook

The performed statistical analysis in Sec. 4.1 concerning significant influences might be continued and intensified. Instead of testing if the slope is 1 for different laser power or different read out days, a t-test might be more appropriate. Also "read out day" should be considered a categorial variable and an analysis of covariance rather than a regression could be performed. Regarding the error estimation of the mean intensities μ_l in one LET level (cf. Sec. 4.3), the student t-distribution (or a bootstrap approach) might be more suitable when estimating the confidence interval (standard uncertainty) for intra- and inter-detector variability, due to the small number of data. Furthermore, the distribution of energy loss observed in Fig. 4.3 with a potential dependency on the particle charge Z_p could be studied.

Since the major source of variability in the utilized detector set was determined to be the inter-detector fluctuations, it would be of particular interest to minimize this source of uncertainty. One possible approach would be to irradiate the same detector with different LET radiation and evaluate the measured fluorescence signals. In such a mixed LET detector, the source of variability caused by different detectors is minimized. However, this approach is limited due to the fact that not any number of different LETs can be utilized, since the different track spots on the detector have to be assignable to the corresponding LETs. It would be realistic to irradiate the same detector with three or four different LETs and to determine for each mixed LET detector a LET-fluorescence relation. Due to different sensitivities of the detectors, this would not result in an entire relation but rather in a "ladder-like approach". Quantifying the detector sensitivity would enable to normalize all single steps and to establish an entire LET-fluorescence relation.

A further approach, which is rather related to the sensitivity of the detectors than to the inter-detector fluctuations, is to perform further investigations of the signal to background relation. It would be of interest to see if the detector background shows (a) a similar pattern of variability and (b) if the relation of background and sensitivity is unambiguous in a way that allows to use the first as an estimator for the latter. Initial measurements regarding the measured background signals within different detectors can be found in Fig. C.2 (cf. App. C).

Finally, it is important to stress that the results in this thesis apply for the specific set of detectors studied. Whether it is correct to deduce any properties of FNTD detectors in general remains to be investigated.

Appendices

A Performed irradiations

Table A.1 – Performed irradiations at HIT - given are the used particle type, the energy, the FWHM of the beam focus, the LET in Al_2O_3, the fluence, and the detector id.

ion type	energy [$\frac{\text{MeV}}{\text{u}}$]	$\text{FWHM}_{\text{focus}}$ [mm]	LET [$\frac{\text{keV}}{\mu\text{m}}$]	fluence [$\frac{1}{\text{cm}^2}$]	detector id
1H	221.06	8.1	1.385	2 x 10^6	hm1101,hm2101,hm4101
	150.41	11.2	1.779	2 x 10^6	hm1102,hm2102,hm4102
	100.46	15.7	2.371	2 x 10^6	hm1103,hm2103,hm4103
	68.08	23.5	3.179	2 x 10^6	hm1104,hm2104,hm4104
	48.12	32.4	4.166	2 x 10^6	hm1105,hm2105,hm4105
4He	216.7	4.9	5.622	2 x 10^6	hm1106,hm2106,hm4106
	140.14	7.1	7.489	2 x 10^6	hm1107,hm2107,hm4107
	93.51	10.0	10.02	2 x 10^6	hm1109,hm2109,hm4109
12C	430.1	7.8	33.91	2 x 10^6	hm1112,hm2112,hm4112
	281.57	8.1	42.18	2 x 10^6	hm1113,hm2113,hm4113
	175.1	9.1	56.70	2 x 10^6	hm1114,hm2114,hm4114
	143.79	9.8	64.74	2 x 10^6	hm1115,hm2115,hm4115
	118.52	10.6	74.29	2 x 10^6	hm1116,hm2116,hm4116
	91.14	11.9	90.16	2 x 10^6	hm1117,hm2117,hm4117
16O	430.32	2.7	61.34	1 x 10^6	hm1118,hm2118,hm4118
	294.58	3.6	74.49	1 x 10^6	hm1120,hm2120,hm4120
	384.27	2.8	64.74	2 x 10^6	hm1119,hm2119,hm4119
	182.62	5.2	99.72	2 x 10^6	hm1122,hm2122,hm4122
	156.71	6.1	110.4	2 x 10^6	hm1123,hm2123,hm4123
	139.09	6.8	120.0	2 x 10^6	hm1124,hm2124,hm4124
	119.73	7.8	133.6	2 x 10^6	hm1125,hm2125,hm4125
	103.77	8.8	148.2	2 x 10^6	hm1126,hm2126,hm4126

B Performed read outs

Table B.1 – Read out parameters for LSM710 - given are the laser and objective type, the number of rescans R, the dwell time τ, the pinhole diameter d_{pinhole}, the digital gain g and offset Δg, the frame and image size and the colour depth.

Laser type	helium-neon laser (633 nm)
objective type	63x/1.40 Oil DIC M27
relative laser power p	variable
number of rescans R	1
dewll time τ	40.34 µs
pinhole diameter d_{pinhole}	1 AU
digital gain g	0.2
digital offset Δg	0
frame size	1280×1280 pixel
image size	$134.8 \times 134.8\,\mu\text{m}^2$
colour depth of the image	16 Bit

Table B.2 – Performed read outs with LSM710 - given are the read out cycle, the ion type, the LET in Al_2O_3, detector id, the read out day, the region, the laser power p, the dwell time τ, the number of rescans R and the read out depth z.

read out	ion type	LET [$\frac{keV}{\mu m}$]	det id	read out day	regions	p [%]	τ [µs]	R	z [µm]
2nd	1H	1.385	hm2101	6	4	100	40.34	1	30
		1.779	hm2102	6	4	100	40.34	1	30
		2.371	hm1103	9	4	100	40.34	1	30
			hm2103	6	4	100	40.34	1	30
			hm4103	9	4	100	40.34	1	30
		3.179	hm2104	6	4	100	40.34	1	30
		4.166	hm2105	6	4	100	40.34	1	30
	4He	5.622	hm2106	6	4	60;100	40.34	1	30
		7.489	hm1107	9	4	25;100	40.34	1	30
			hm2107	6	4	25;100	40.34	1	30
			hm4107	9	4	25;100	40.34	1	30
		10.02	hm2109	6	4	25;100	40.34	1	30
	12C	33.91	hm1112	8	4	10;100	40.34	1	30
			hm2112	5	4	10;100	40.34	1	30
		42.18	hm1113	8	4	10;100	40.34	1	30
			hm2113	5	4	10;100	40.34	1	30
		56.70	hm1114	8	4	10;100	40.34	1	30
			hm2114	5	4	10;100	40.34	1	30
		64.74	hm1115	8	4	10;100	40.34	1	30
			hm2115	5	4	10;100	40.34	1	30
			hm4115	8	4	10;100	40.34	1	30
		74.29	hm1116	8	4	10;100	40.34	1	30
			hm2116	5	4	10;100	40.34	1	30
			hm4116	8	4	10;100	40.34	1	30
		90.16	hm1117	8	4	10;100	40.34	1	30
			hm2117	5	4	10;100	40.34	1	30
	16O	61.34	hm1118	7	4	7;100	40.34	1	30
			hm2118	4	4	7;100	40.34	1	30
		74.49	hm1120	7	4	7;100	40.34	1	30
			hm2120	5	4	7;100	40.34	1	30
			hm4120	9	4	7;100	40.34	1	30
		64.74	hm1119	7	4	7;100	40.34	1	30
			hm2119	4	4	7;100	40.34	1	30
			hm4119	9	4	7;100	40.34	1	30
		99.72	hm1122	7	4	7;100	40.34	1	30
			hm2122	4	4	7;100	40.34	1	30
		110.4	hm1123	7	4	7;100	40.34	1	30
			hm2123	5	4	7;100	40.34	1	30
		120.0	hm1124	7	4	7;100	40.34	1	30
			hm2124	4	4	7;100	40.34	1	30
		133.6	hm1125	7	4	7;100	40.34	1	30
			hm2125	4	4	7;100	40.34	1	30
			hm4125	7	4	7;100	40.34	1	30
		148.2	hm1126	4	4	7;100	40.34	1	30
			hm2126	4	4	7;100	40.34	1	30
			hm4126	4	4	7;100	40.34	1	30
1st	16O	61.34	hm1118	2	6	10	40.34	1	30
			hm2118	2	6	7	40.34	1	30
			hm4118	2	6	15	40.34	1	30
		64.74	hm2119	3	4	13	40.34	1	30
		99.72	hm2122	3	4	8	40.34	1	30
		120.0	hm2124	3	4	8	40.34	1	30
		133.6	hm2125	3	4	8	40.34	1	30
		148.2	hm1126	1	6	7	40.34	1	30
			hm2126	1	6	7	40.34	1	30
			hm4126	1	6	7	40.34	1	30

C Background measurements

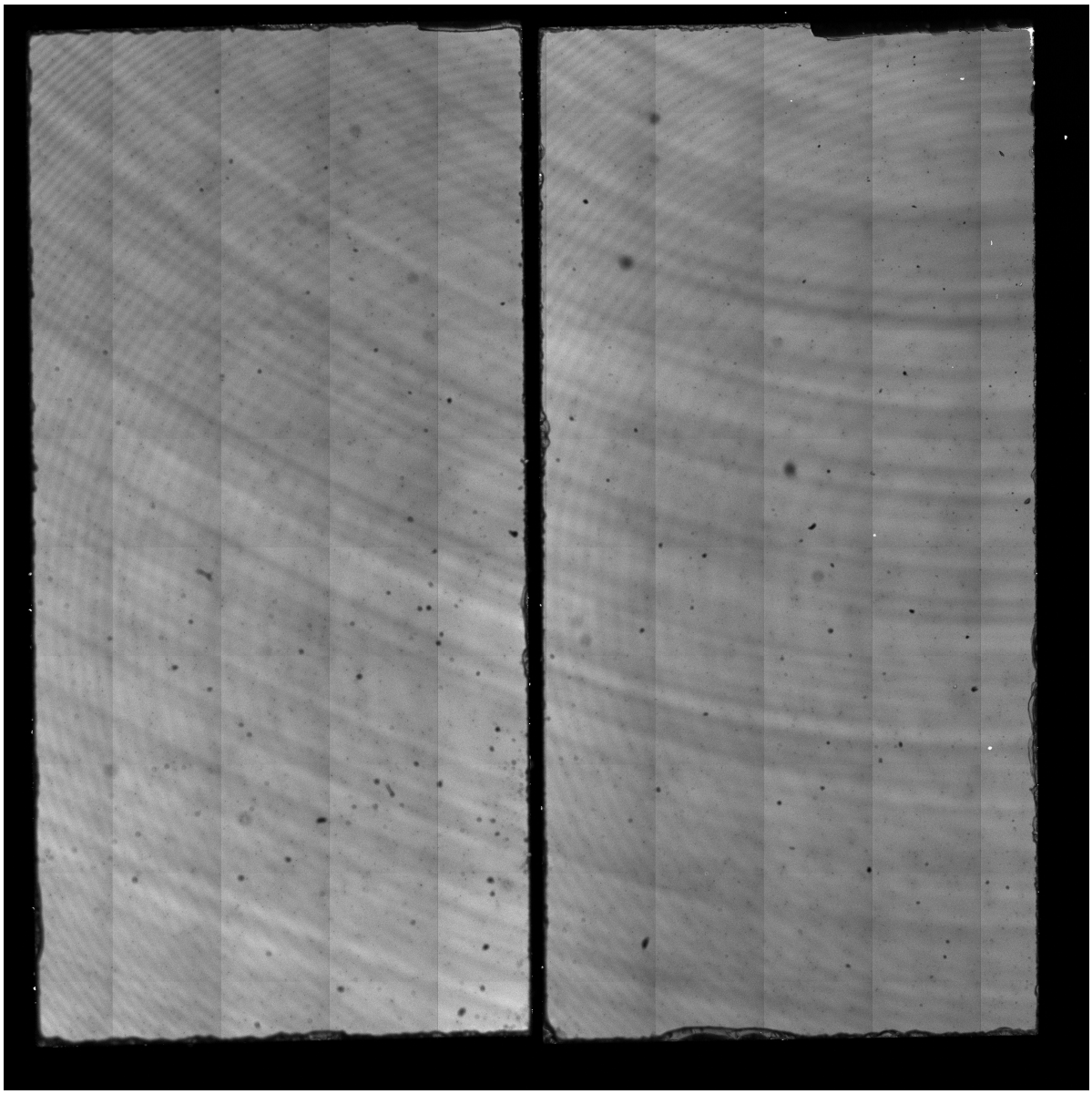

Figure C.1 – Complete Background image of two unirradiated detectors. The objective EC Plan-Neofluar 10x/0.30 M27, a frame size of 1024×1024, a dwell time $\tau = 25.21\,\mu$s, the read out depth $z = 50\,\mu$m, and the laser power $p = 50\%$ were utilized. The entire image consists of 10 horizontal and 10 vertical tile scans resulting in a total size of $8501.92 \times 8501.92\,\mu\text{m}^2$. The nature of the observed circular fluctuations is not yet known. The single tile scans of the microscope are easily distinguishable, since the flat field of the microscope leads to a marginal reduction in the measured intensities.

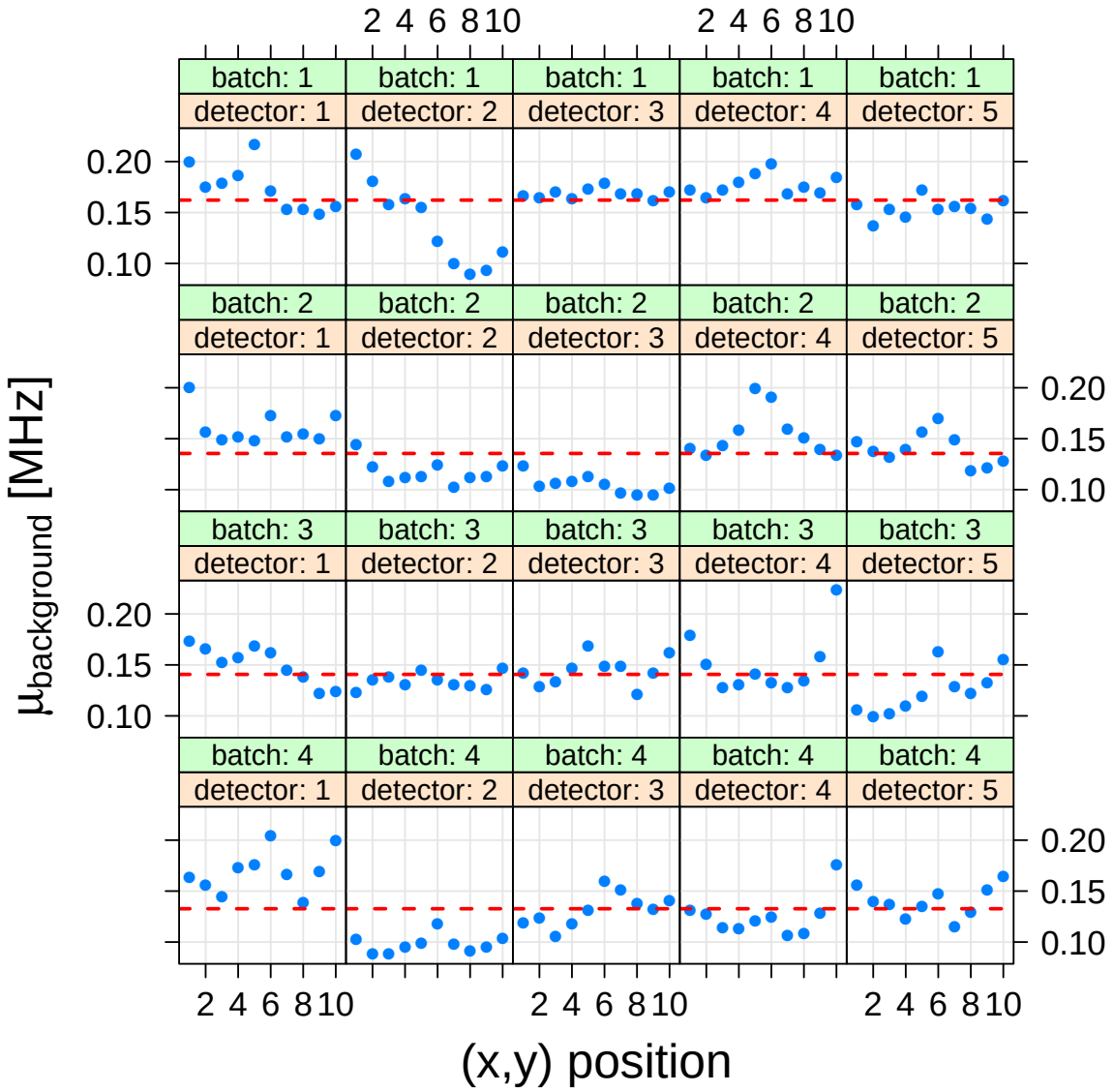

Figure C.2 – Mean Background measurements on 10 different positions within the detectors. The objective 63x/1.40 Oil DIC M27, a frame size of 512x512, a dwell time $\tau = 50.42\mu$s, the read out depth $z = 30\mu$m and the laser power $p = 100\%$ were utilized.

D Internship report

Project Internship [1]

Henning Mescher

[1] performed at DKFZ, research group: E0409, period: 03.03.14 - 04.04.14

1 Introduction

From the beginning to the end of March I completed a Project Internship at DKFZ. My task was the exemplary establishment of a linear energy transfer (LET) calibration curve using already irradiated fluorescent nuclear track detectors (FNTDs). The calibration curve correlates the count rate of a FNTD with the LET of the penetrating particle. Such a correlation was already observed for higher LETs [1]. To perform own measurements and to establish a precise calibration is the topic of my Bachelor's thesis, which is going to start directly afterwards. Thus, I could use the Project Internship to get familiar with the issue of my future work. Furthermore, I made a lot of new and interesting experiences. Examples for this are the weekly group meetings, where group members discuss their specific problems with the entire group, the read out routine of the confocal microscope and the irradiations with heavy ions at the Heidelberg Ion-Beam Therapy Center (HIT).

2 Initial Steps

The fluorescence signal of a FNTD is obtained by confocal detector read out. The received data is analyzed by the programs *ImageJ* and *R*. Therefore, it is essential to get familiar with those programs. Understanding and learning the functions of the programs, especially of the statistic program *R*, took most of the time during the first three weeks. Nonetheless, this process is not finished yet. In addition, primarily in the beginning of the internship, I read a few papers about FNTDs and also about basic quantities in medical physics to get an overview about the theoretical background.

3 LET calibration curve

To analyze where problems may occur and to produce the most effective workflow concerning the establishment of the calibration curve, I used already performed measurements and evaluated them. The measurements include irradiations of FNTDs with three different kinds of ions (1H, 4He, 12C). Due to different initial energies of the ions this results in eight measurements with different LET values.
During irradiation with ionizing particles, color centers inside the FNTD undergo the radiochromic transformation by capturing secondary electrons. Those transformed color centers have different absorption and emission bands compared to the untransformed background. The larger the LET of the particle, the more color centers undergo the transformation. Thus, the particle's track and its energy loss can be measured with a confocal microscope using the fluorescence amplitude or the fluorescence count rate of the detector.

3.1 Track position determination

The received images from the confocal microscope were evaluated first with *ImageJ*. This allows to get the track positions of each single particle using an *ImageJ* plugin which was developed by the MOSAIC group. Besides the approximately radius of the track spots, this plugin needs also a cut-off value for the non-particle discrimination and a percentile that determines which bright pixels are accepted as particles.

3.2 Fluorescence amplitude measurement

For further analysis the statistic programm *R* was used. A fit routine from the FNTD package for *R* (which was developed in our group) allows to fit every single particle track with a gaussian function. Therefore, the routine needs only the raw data (microscope images) and the single track positions (derived from *ImageJ*). The amplitude of the gaussian fit indicates the fluorescence amplitude of the corresponding track. The fluorescence amplitude of the same particles with equal LET values may vary due to stochastic processes. For this reason, the mean value of the gauss amplitudes in one image slice is calculated. Thus, one receives eight data points with different intensities corresponding to eight different LET values.

3.3 Microscope correction

However, the fluorescence amplitude is also dependent on microscopic parameters and on the saturation of the avalanche photodiodes (APDs). The important microscopic parameters are the laser power p, the dwell time τ, the number of rescans N and the read out depth z. All detectors were read out with full laser power and only one scan at a fixed depth of 30 µm to prevent effects of those parameters. Thus, the intensity values have to be corrected only for different dwell times. By dividing the mean counts (mean fluorescence amplitude) by the dwell times one gets the fluorescence count rates. The correction function from Martin's paper [2] is used to get the actual count rates concerning the saturation of the APDs. Further microscopic corrections such as flat field or spherical aberrations will be considered in the Bachelor's thesis.

3.4 Fit result

The result of this first LET calibration curve is shown in figure 1. The LET values were calculated with *SRIM* for Al_2O_3 using the energy per nucleon and the corresponding Z value which is known from the irradiation.

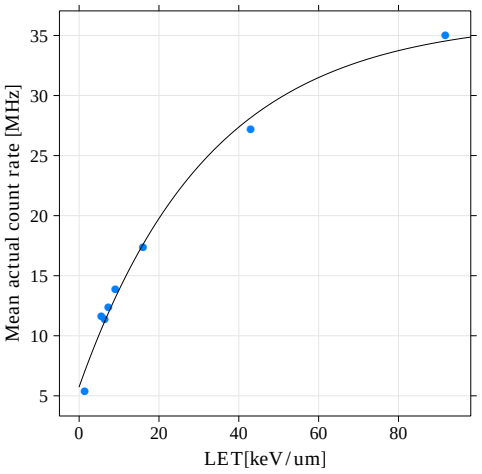

Figure 1 – Mean actual count rate of a track spot in dependency on the LET in Al_2O_3 with fit

In spite of the applied corrections, the course of the measured values suggests a saturation. This result and the high count rates lead to the assumption that either the saturation correction (APDs) is too inaccurate or the detector is saturated itself. Hence, a APD saturation function $g(x)$ with the following results is fitted to the experimental points:

$$g(x) = A - B \cdot e^{-x/k} \quad A_{fit} \approx 36.4 \text{ MHz} \quad B_{fit} \approx 30.6 \text{ MHz} \quad k_{fit} \approx 32.7 \frac{\text{keV}}{\mu\text{m}} \tag{1}$$

The saturation course of the measured values indicates, that measurements with a lower laser power may yield a better result.

3.5 Background influence

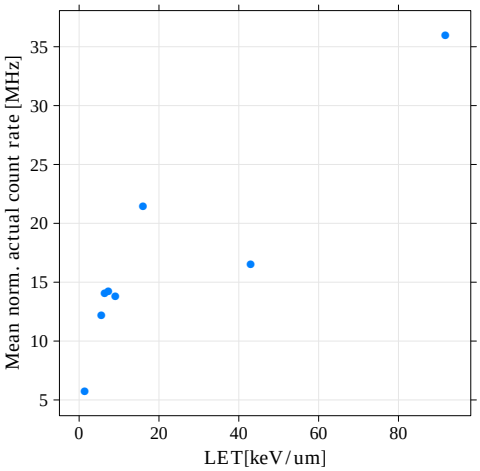

Figure 2 – Mean actual count rate of a track spot normalized to the mean background in dependency on the LET in Al_2O_3

Besides stochastic processes and microscope parameters the coloration of the detectors may also have an influence on the measured fluorescence intensities. Figure 2 shows an attempt to include the coloration of the detector to the correction. For this purpose the count rates are normalized to the mean background signal of all detectors. The result is not that satisfying, especially because the second last measured value no longer fits to the other values. Anyway, this kind of background normalization is very complicated because the background signal is not only a simple offset in the detected signal but it is also dependent on other quantities of the used particles (e.g. LET).
To exclude problems with different colorations, it is planed to use detectors with the same color center density for the calibration measurements.

4 Confidence Interval

The calibration curve shall be used to determine the LET from a measured fluorescence count rate. Mathematically, the LET itself is easy to determine using the inverse calibration function. For a calibration function $f(x, \Phi_n)$ with parameters Φ_n and LET x, the specific LET x_λ for a given fluorescence count rate λ is calculated by:

$$y = f(x, \Phi_n) \quad \Rightarrow \quad x_\lambda = f^{-1}(\lambda, \Phi_n) \tag{2}$$

Of particular interest is the uncertainty of this determination. To calculate the confidence interval (CI) of such an inverse problem, there are a few different approaches which are shortly introduced in the following. The basis forms thereby the dissertation of Xiaoqi Jiang [3], which provides an excellent summary of the different methods.

4.1 Delta-Method

The Delta-Method uses the inverse function of equation (2) and calculates the variance of it:

$$x_\lambda = f^{-1}(\lambda, \Phi_n) = h(\Phi_n) \quad \text{with} \quad \text{var}(h(\Phi_n)) \approx \nabla h(\Phi_n)^T \cdot \Sigma \cdot \nabla h(\Phi_n) \tag{3}$$

Here is Σ the variance-covariance matrix of the parameters and T indicates the transposition of the vector $\nabla h(\Phi_n)$. Using this result and the quantile $t_{(1-\alpha/2)}$ from the Student t Distribution, the CI is given by:

$$\hat{x}_\lambda \quad \pm \quad t_{(1-\alpha/2)} \sqrt{\text{var}(h(\hat{\Phi}_n))} \tag{4}$$

The hat indicates that the estimated parameters (obtained by the calibration fit to the measured values) are used.

4.2 Wald-Method

The Wald-Method first reparameterizes the initial calibration function. In this process, using the condition of a given fluorescence count rate λ, one parameter is replaced by the wanted LET value x_λ. This new function f^{rep} is now fitted to the data and one receives an estimation of the error in the LET. If the calibration function f is for example of a linear type it follows:

$$f(x, \Phi_n) = \Phi_1 x + \Phi_2 \quad , \quad \lambda = \Phi_1 x_\lambda + \Phi_2 \quad \Rightarrow \quad f^{rep}(x, x_\lambda, \Phi_2) = \frac{\lambda - \Phi_2}{x_\lambda} x + \Phi_2 \tag{5}$$

From the fit of f^{rep} to the data, one obtains the standard deviation $\sigma(\hat{x}_\lambda)$ of the parameter. Using this estimate it arises for the CI:

$$\hat{x}_\lambda \quad \pm \quad t_{(1-\alpha/2)} \sigma(\hat{x}_\lambda) \tag{6}$$

4.3 Bootstrap

The Bootstrap method utilizes resampling of the measured data. A measured data set (x_i, y_{ij}) consists of x_i different LETs and y_{ij} corresponding measured fluorescence count rates. The index j indicates that for every x_i $j = 1, \cdots, n_i$ different fluorescence count rates y_{ij} are measured. The performed irradiations result in eight images from the confocal microscope with different LET x_i ($i = 1, \cdots, 8$). Every image consists of approximately $n_i \approx 200$ usable track spots. Thus, the used data set consists of about 1600 measurements. Using the Bootstrap method, a

bootstrap sample y_i^β, consisting of one y_i for every LET level i, is generated from the original observation. The resampling is done for $\beta = 1, \cdots, b$ with the boot size b indicating the number of generated samples. Those new samples and the x_i form the bootstrap data sets (x_i, y_i^β). The reparameterized function f^{rep} with x_λ as parameter is fitted to each of the resampled data sets. Thus, one receives for every resampling an estimate of the LET value. Using the distribution of those LET values enables to assess the CI. Concerning the generation of the bootstrap sample, a distinction is made between the non-parametric and the parametric Bootstrap.

4.3.1 Non-parametric Bootstrap

The non-parametric Bootstrap uses the entire data which is obtained by the read out with the confocal microscope. This means it utilizes every fluorescence count rate y_{ij}, which is measured in one of the eight images, to resample the measurements. For a new data set one y_{ij} is sampled with replacement for each LET level i.

4.3.2 Parametric Bootstrap

The parametric Bootstrap uses the calibration fit and the mean values $y_i = \overline{y_{ij}}$ of the measured fluorescence count rates, which is determined for every image. For a new data set the residual E_i for each x_i is determined:

$$E_i = y_i - f(x_i, \hat{\Phi}_n) \tag{7}$$

For each x_i one residual E_i is sampled with replacement. To generate a bootstrap sample, those sampled residuals E_i^β are added up to the corresponding value of the fit function:

$$y_i^\beta = f(x_i, \hat{\Phi}_n) + E_i^\beta \tag{8}$$

The non-parametric approach is more general, since it considers the possibility of a LET dependent spread of the measured fluorescence count rates. This spread is neglected in the parametric Bootstrap, as the size of residuals is considered to be equal for every LET. Nonetheless, in the non-parametric case a broad distribution of parameters is expected by using the entire measured values.

5 Simulation

For the experimental setup it is important to know how the precision of the LET determination depends on the number of measured LET levels (x data size) and the number of measured tracks on the detector (y data size). For this reason, a small simulation was performed in *R*.

5.1 Data set generation

A data set with variable x and y data sizes was generated. Thereby it was used a LET dependent spread of the simulated measured values in order to take into account the underlying physical process[2]. The generated data underlies three different kinds of calibration curves: Linear, quadratic and exponential. Each generated data set is fitted with the corresponding fit function.

[2] with rising LET the variation of the fluorescence count rate due to stochastically processes decreases

5.2 Determination of CIs

For a given fluorescence count rate λ, the corresponding value x_λ is calculated. To investigate the precision of this value all different types of CIs which were introduced in section 4, are determined. Figure 3 shows the relative sizes of the CIs in dependency on the x and y data sizes exemplary for the quadratic case. The results for the other function types were qualitatively comparable.

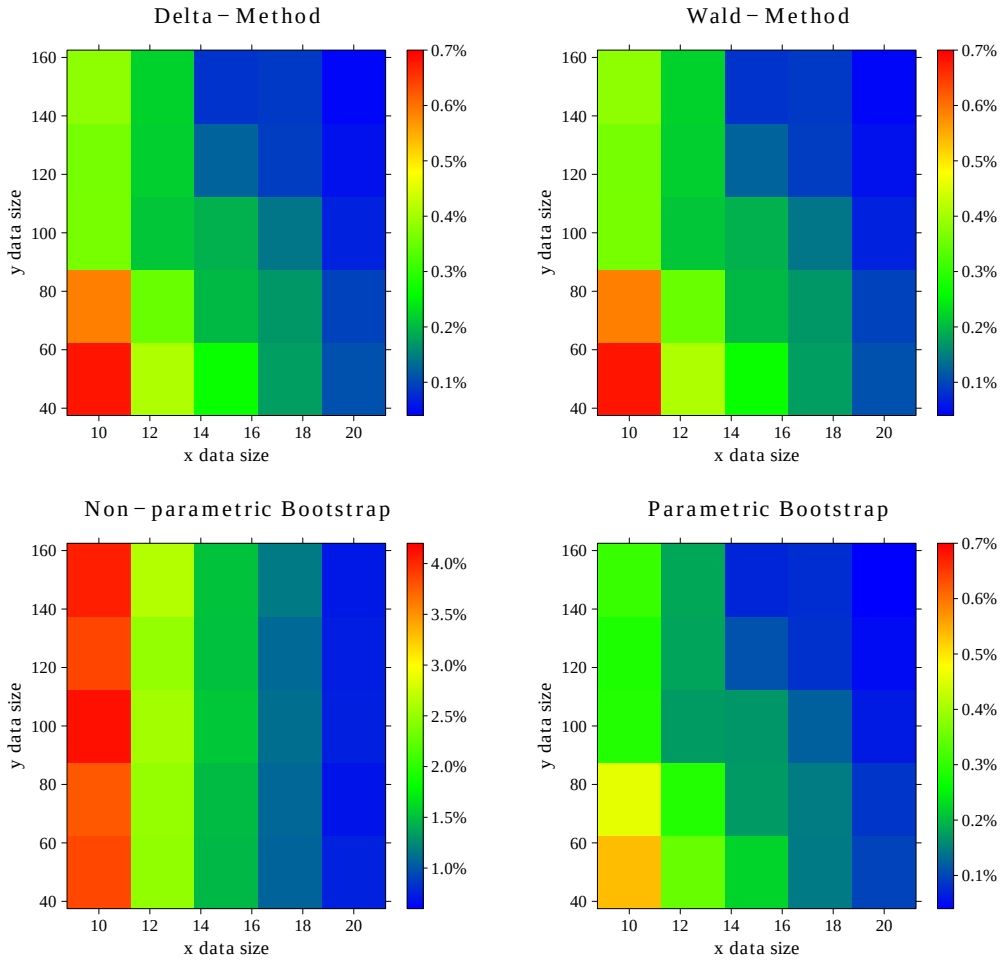

Figure 3 – Relative size of CIs using the different approaches of section 4 (exemplary represented for the quadratic case), a different color scale is used for the non-parametric Bootstrap since the CI rises in this case up to 4 percent

In all cases, the precision of the LET determination increases with rising x and y data sizes. Furthermore, one recognizes that the relative sizes of the CIs obtained by using the Delta- and the Wald-Method are in high agreement. Also the CIs, calculated with the parametric Bootstrap, fits to the other results. Only the CIs determined by the non-parametric Bootstrap deviate enormously from the other results. That is why in this case another color scale is used.

5.3 Non-parametric Bootstrap

The deviation of the non-parametric Bootstrap CIs is caused by the different resampling method which is used to generate the bootstrap samples. As it is described in section 4, the parametric Bootstrap uses the mean fluorescence count rates and the residuals to get a new data sample. Therefore, the sampled values do not deviate so much from the applied calibration function. Concerning the non-parametric case, where every measured count rate is possible to be sampled, it is different. Thus, it is for example possible that for two adjacent LET levels once the maximum ($y_{i,j_{max}}$) and once the minimum ($y_{i\pm1,j_{min}}$) is selected. Due to this the sampled values may deviate much more from the calibration fit function than in the parametric case. The result is that the distribution of the LET values, obtained by fitting every resampled data, is much wider and the CIs increase dramatically.

Both types use quantiles to determine the median value and the CI. With the assumption that the LET values are normally distributed, one can chose the mean value and the standard deviation as an attempt to determine the CI. In this case, one obtains the CI due to the error of the mean value. This means that the standard deviation of the distribution has to be devided by the square root of the number of LET values which form the distribution. The result of this approach is shown in figure 4. However, in this case the CIs are much smaller compared with the other methods. On the basis of the large deviation of the CIs calculated with the non-parametric Bootstrap from the other results, this method seems not to be the right choice.

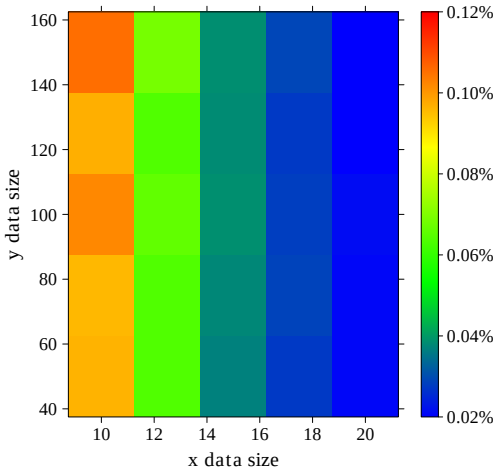

Figure 4 – Relative size of CIs using the error of the mean value in the non-parametric case

Altough the result of the parametric Bootstrap is comparable to the Delta- and the Wald-Method, this method is linked to the condition of a similar spread of the measured count rates for every LET. Finally the most robust Methods seems to be the Delta- and the Wald-Method. Nonetheless, the final choice have to be done when more information about the measured data is available.

5.4 Bootstrap size

Besides the x and the y data sizes, which are interesting for the experimental setup, the boot size b for the bootstrap methods is an important parameter too. The boot size specifies the number of resampled data sets and thus the number of LET values for the distribution. This means that the boot size is a question of calculation time. Figure 5 shows the relative sizes of the CIs for the biggest y and x data sizes in dependency of the boot size exemplary for the parametric Bootstrap. In fact there is no significant trend concerning the boot size. Nonetheless, there is a lower limit. Under this limit the number of LET values is not sufficient to obtain good statistics.

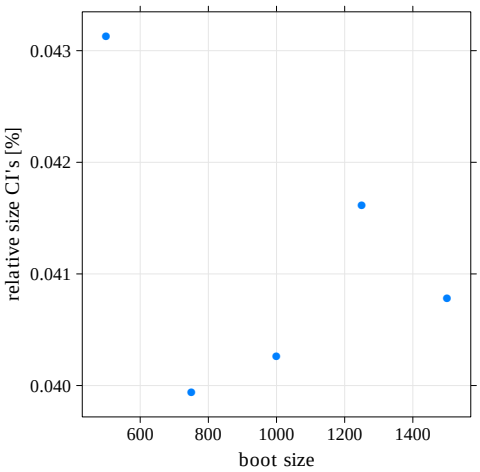

Figure 5 – Relative size of CIs in dependency of the bootstrap size exemplary for the parametric Bootstrap

6 Conclusion

Besides learning basics in programming with the statistic program R, this internship gave me a deep insight into the scientific work of a research group at DKFZ. As I mentioned at the beginning, especially the group meetings were a new experience for me. During the work experience I was able to investigate where problems of future measurements may occur. As a result, the next measurements will be performed with a much lower laser intensity to prevent saturation effects. The error source of different colorizations is hopefully removed by track detectors with equal color center densities. The simulation concerning the experimental setup results in a clear tendency that larger x and y data sizes lead to a higher precision in the LET determination. Furthermore, without more information about the measured data, it is not useful to choose one of the presented methods concerning the confidence intervals.
I look forward to future measurements to establish a precise calibration based on my own results.

References

[1] Sykora, G.J., Akselrod, M.S., Benton, E.R., Yasuda, N., 2008. Spectroscopic properties of novel fluorescent nuclear track detectors for high and low LET charged particles. Radiat. Meas. 43, 424-426.

[2] Niklas, M., Melzig, C., Abdollahi, A., Bartz, J., Akselrod, M.S., Debus, J., Jäkel, O., Greilich, S., 2013. Spatial correlation between traversal and cellular response in ion radiotherapy - Towards single track spectroscopy. Radiat. Meas. 56, 286-288.

[3] Xiaoqi Jiang, 2013. Estimation of effective concentrations from in vitro dose-response data using the log-logistic model. Ruprecht-Karls-Universität Heidelberg, 13-20.

[4] Venables, W.N., Smith, D.M., R Core Team, 2013. An Introduction to R.

List of Figures

List of Tables

Bibliography

[1] Particle Therapy Co-Operative Group (PTCOG). Statistics of patients treated in particle therapy facilities worldwide. `http://www.ptcog.ch/index.php/ptcog-patient-statistics` (2014).

[2] IAEA, ICRU. Relative Biological Effectiveness in Ion Beam Therapy. Technical Report 461, International Atomic Energy Agency and International Commission on Radiation Units and Measurements, 2008.

[3] J.-M. Osinga, M.S. Akselrod, R. Herrmann, V. Hable, G. Dollinger, O. Jäkel, and S. Greilich. High-accuracy fluence determination in ion beams using fluorescent nuclear track detectors. *Radiation Measurements*, 56:294–298, 2013.

[4] G. J. Sykora, M.S. Akselrod, E.R. Benton, and N. Yasuda. Spectroscopic properties of novel fluorescent nuclear track detectors for high and low let charged particles. *Radiation Measurements*, 43:422–426, 2008.

[5] M. Niklas, C. Melzig, A. Abdollahi, J. Bartz, M.S. Akselrod, J. Debus, O. Jäkel, and S. Greilich. Spatial correlation between traversal and cellular response in ion radiotherapy e towards single track spectroscopy. *Radiation Measurements*, 56:285–289, 2013.

[6] Hanno Krieger. *Strahlungsmessung und Dosimetrie*. Vieweg+Teubner, 2011.

[7] ICRU. Fundamental quantities and units for ionizing radiation (revised). Technical Report 85, International Commission on Radiation Units and Measurements, ICRU, 7910 Woodmont Avenue, Bethesda, Maryland 20814, USA, October 2011.

[8] D. Schardt, T. Elsässer, and D. Schulz-Ertner. Heavy-ion tumor therapy: Physical and radiobiological benefits. *Reviews of Modern Physics*, 82, 2010.

[9] ICRU. Stopping Powers and Ranges for Protons and Alpha Particles. Technical Report 49, International Commission on Radiation Units and Measurements, ICRU, 7910 Woodmont Avenue, Bethesda, Maryland 20814, USA, 1993.

[10] Martin Anthony Niklas. *Cell-fluorescent ion track hybrid detector: A novel hybrid technology for direct correlation of single ion tracks and subcellular damage sites in clinical ion beam*. PhD thesis, University of Heidelberg, 2014.

[11] Mark S. Akselrod, R.C. Yoder, and Gleb M. Akselrod. Confocal fluorescent imaging of tracks from heavy charged particles utilising new al2o3:c,mg crystals. *Radiation Protection Dosimetry*, 119:357–362, 2006.

[12] G. M. Akselrod, M. S. Akselrod, E. R. Benton, and N. Yasuda. A novel Al2O3 fluorescent nuclear track detector for heavy charged particles and neutrons. *Nuclear Instruments and Methods in Physics Research B*, 247:295–306, 2006.

[13] M. Niklas, S. Greilich, C. Melzig, M.S. Akselrod, J. Debus, O. Jäkel, and A. Abdollahi. Engineering cell-fluorescent ion track hybrid detectors. *Radiation Oncology*, 8:141, 2013.

[14] Mark S. Akselrod and Anne E. Akselrod. New al2o3:c,mg crystals for radiophotoluminescent dosimetry and optical imaging. *Radiation Protection Dosimetry*, 119:218–221, 2006.

[15] Mark S. Akselrod, Anne E. Akselrod, Sergei S. Orlov, Subrata Sanyal, and Thomas H. Underwood. Fluorescent aluminum oxide crystals for volumetric optical data storage and imaging applications. *Journal of Fluorescence*, 13:503–511, 2003.

[16] Grischa Klimpki. Towards in-vivo ion range measurements using fluorescent nuclear track detectors. Bachelor's thesis, University of Heidelberg, 2012.

[17] M. S. Akselrod and G. J. Sykora. Fluorescent nuclear track detector technology - a new way to do passive solid state dosimetry. *Radiation Measurements*, 46:1671–1679, 2011.

[18] Garrett Jeff Sykora and Mark S. Akselrod. Photoluminescence study of photochromically and radiochromically transformed al2o3:c,mg crystals used for fluorescent nuclear track detectors. *Radiation Measurements*, 45:631–634, 2010.

[19] G. J. Sykora, M. Salasky, and M. S. Akselrod. Properties of novel fluorescent nuclear track detectors for use in passive neutron dosimetry. *Radiation Measurements*, 43:1017–1023, 2008.

[20] Guy Cox. *Optical Imaging Techniques in Cell Biology*. Number ISBN 0-8493-3919-7. CRC Press, Taylor & Francis Group, 2007. S. 57-75.

[21] Carl Zeiss MicroImaging GmbH. LSM 710 - The Power of Sensitivity. `http://www.zeiss.de/sensitivity` (2014).

[22] Carl Zeiss MicroImaging GmbH. *Operating Manual - LSM 710 and ConfoCor 3*, April 2009.

[23] W. S. Rasband. ImageJ. `http://rsb.info.nih.gov/ij/` (2014).

[24] Sebastian Hoof. Correlation of particle and background signal in al2o3:c,mg fluorescent nuclear track detectors. Bachelor's thesis, University of Heidelberg, 2013.

[25] R Development Core Team. *R: A Language and Environment for Statistical Computing*. R Foundation for Statistical Computing, Vienna, Austria, 2010. ISBN 3-900051-07-0.

[26] James F. Ziegler. SRIM - The Stopping and Range of Ions in Matter. `http://www.srim.org` (2014).

[27] S. Greilich, J.-M. Osinga, M. Niklas, F.M. Lauer, G. Klimpki, F. Bestvater, J.A. Bartz, M.S. Akselrod, and O. Jäkel. Fluorescent nuclear track detectors as a tool for ion-beam therapy research. *Radiation Measurements*, 56:267–272, 2013.

[28] S. Greilich, J.-M. Osinga, M. Niklas, F.M. Lauer, F. Bestvater, and O. Jäkel. Quantitative read-out of al2o3:c,mg-based fuorescent nuclear track detectors using a commercial confocal microscope. preprint available at `arXiv:1407.0986[physics.ins-det]` (2014).

Acknowledgements

I am deeply grateful for the support I obtained during this thesis and want to thank all people at the DKFZ and the Department of Physics and Astronomy of the University in Heidelberg for giving me the opportunity to work at this project. I would like to express my gratitude to Prof. Dr. Oliver Jäkel, the Head of the Department of Medical Physics in Radiation Oncology at the DKFZ, for accepting me as Bachelor student in his research group and for being my supervisor and second referee. Furthermore, I would like to thank Prof. Dr. Peter Bachert for being my first referee and the representative of the Department of Physics and Astronomy.

Concerning the project and the thesis, my special thanks goes to Dr. Steffen Greilich. He never got tired in discussing and explaining certain aspects referring to the project. Furthermore, he provided my work week after week with new ideas and new interesting approaches. Without his outstanding support, writing this thesis would have been impossible. In addition, I have to thank the Heavy Ion Therapy Research Group for an excellent working atmosphere. A very special thanks is due to Grischa Klimpki, who encourage my work day after day. He never considered himself too good for investing time to support me in solving my problems. He also performed all irradiations with me at HIT, and gave me an introduction to the confocal detector read out.

I want to thank Dr. Mark S. Akselrod from Landauer Inc. for providing my project with FNTDs and Dr. Felix Bestvater from the light microscopy facility at DKFZ for supplying myself with enough read out times. Additionally I would like to give thanks to Dr. Stephan Brons from HIT for technical assistance during the irradiations.

In the end, I would like to thank my family for supporting me during writing this thesis, and thank especially my parents who made it possible to study physics in Heidelberg without any pressure. Finally, I want to thank my girlfriend for supporting me over the last weeks of this thesis.

Erklärung

Ich versichere, dass ich diese Arbeit selbstständig verfasst und keine anderen als die angegebenen Quellen und Hilfsmittel benutzt habe.
Heidelberg, den